

Politecnico
di Torino

Politecnico di Torino

Master's Degree in Energy and Nuclear Engineering

Non-Linear Modelling of the Froude-Krylov Forces in a Point-Absorber Wave Energy Converter

An Extension to Spherical and Spline-Based Geometries

Supervisor:
Prof. Giuseppe Giorgi

Candidate:
Egidio Francesco Flaminio

A.Y. 2025/2026

Abstract

The design and performance analysis of wave energy converters (WECs) require mathematical models that are both accurate and computationally efficient. Under marine conditions that cause large excursions of the buoy, the assumption of small displacements on which linear potential theory is based fails. As the system's behaviour becomes non-linear, the application of linear theory inevitably leads to estimates of the dynamic response and energy output that are inaccurate, overly optimistic or physically unrealistic. The Froude–Krylov (FK) force constitutes the primary and most critical source of hydrodynamic non-linearity for point absorber-type floats. Consequently, a rigorous calculation of the FK pressure integral over the instantaneous effective wetted area of the device is required. However, conventional mesh-based methods often entail unsustainable computational costs, severely limiting their applicability in time-domain simulations or iterative analyses for power take-off (PTO) optimisation. This thesis proposes a computationally efficient approach for calculating non-linear Froude-Krylov forces, applicable to axially symmetric point absorber-type WECs operating in three degrees of freedom (surge, heave and pitch). Using the mathematical framework of the NLFK4ALL toolbox, the study analyses and compares axially symmetric geometries of cylindrical, spherical and spline-generated shapes. The hydrodynamic forces were evaluated using two different strategies: a numerical method based on Simpson's integration and an algebraic solution, which ensures a substantial reduction in computation time. This study aims to bridge the gap between computational efficiency and non-linear hydrodynamic accuracy, with a view to improving the design and optimisation of WECs. The ultimate objective is to support research in the renewable energy sector, promoting a more effective and sustainable exploitation of the energy potential of wave motion.

Contents

1 Introduction **8**
- 1.1 Context and Motivation . . . 8
- 1.2 Thesis objectives . . . 10

2 Theoretical Framework **11**
- 2.1 Potential Flow Theory . . . 11
- 2.2 Hydrodynamics Model of the Floating Body . . . 12
- 2.3 Linear Froude-Krylov Forces . . . 14
- 2.4 Linear Frequency-Domain . . . 15
- 2.5 The NLFK4ALL Mathematical Framework . . . 15
  - 2.5.1 Reference Frames in 3-DoF configuration . . . 16
  - 2.5.2 Intersection and Integration limits . . . 17
  - 2.5.3 Integration . . . 19
  - 2.5.4 Analytical Parameterisation . . . 19
  - 2.5.5 Normalization of the integration domain . . . 20
  - 2.5.6 Geometric Properties Evaluation . . . 20
  - 2.5.7 Nonlinear Froude-Krylov Forces . . . 21
- 2.6 Numerical Integration via 2D Simpson's Rule . . . 22
- 2.7 Closed-Form Algebraic Solutions . . . 23
- 2.8 Irregular Sea States . . . 23
- 2.9 Time-Domain Resolution of the Equation of Motion . . . 24

3 Case Studies and Preliminary Validation under Linear Assumptions **26**
- 3.1 Validation in Linear Condition . . . 26
  - 3.1.1 Hydrostatic Stiffness . . . 27
- 3.2 Geometric Defintion . . . 28
  - 3.2.1 Cylinder . . . 28
  - 3.2.2 Spherical Geometry . . . 29
  - 3.2.3 The Spline-Based Buoy . . . 30
- 3.3 Dynamic Linear Validation . . . 32
- 3.4 Check in Irregular Waves . . . 36

4 Time-Domain Simulations and Performance Analysis **39**
- 4.1 Simulation Setup . . . 39
- 4.2 Free decay test . . . 40
- 4.3 PTO Control Strategies . . . 43
  - 4.3.1 Uncontrolled Response . . . 43
  - 4.3.2 Passive Control . . . 46

4.3.3 Reactive Control 52

5 Conclusion **59**

A Algebraic Solution **61**
A.0.1 Main parameters 61
A.1 General Approach 61
A.2 **Cylinder** 64
A.3 **Cone** 65
A.4 **Disk** 66
A.5 **Sphere** 66
A.6 **Cubic Spline** 67

List of Figures

1.1 Benefits of ocean energy technologies.Adapted from IRENA and OEE (2023) . . 8
1.2 Schematic representation of the Swedish heaving buoy equipped with a direct-drive linear electrical generator. Source: Uppsala University, as cited in [1] 9

2.1 Generic profile of revolution in the BF (left); relative position between frames after displacement (right). 16
2.2 Plot of the flat approximation of the free-surface elevation (blue dotted line) and the exact representation (purple) in WF and BF. 18
2.3 Representation of the WEC as a mass-spring-damper system. Source: [2] 25

3.1 Comparison of the hydrostatic stiffness coefficients in heave ($K_{h_{33}}$) and pitch ($K_{h_{55}}$) for the Cylinder, Sphere, and Spline geometries. 28
3.2 Representation of cylindrical geometry under translations and rotations (a). Discretized mesh (b) for the cylindrical floater. 29
3.3 Representation of spherical geometry (a). Discretized mesh (b) for the spherical floater. 30
3.4 Graphical representation of the revolution profile using nodes of Bèzier for a cubic spline as a function of $f(\rho)$ 31
3.5 Representation of 'SplineBuoy' geometry under translations and rotations in the Word Frame (left) and Body Frame (right). 32
3.6 Comparison of dynamic Froude-Krylov Heave excitation forces at different frequency for the three analyzed geometries. 33
3.7 Frequency-domain comparison of dynamic Froude-Krylov pitch torques for the three analyzed geometries 34
3.8 Comparison of the dynamic Froude-Krylov surge excitation force ($|F_{FK}|$) and its phase for the Spline-based floater. 35
3.9 Time-domain kinematics (top panels) and Froude-Krylov excitation forces (bottom panels) for the spherical floater in a 3-DoF configuration (Surge, Heave, and Pitch) 37
3.10 Comparison of pitch kinematics (top) and excitation moments (bottom) between the Cylinder and the Spline geometries under irregular wave conditions. 38

4.1 Frequency-dependent hydrodynamic coefficients evaluated via the BEM solver (NEMOH) for the Cylinder, Sphere, and SplineBuoy geometries. The top panels illustrate the added mass in heave (A_{33}) and pitch (A_{55}), while the bottom panels show the corresponding radiation damping coefficients (B_{33}, B_{55}). 41
4.2 Free decay test for the cylinder over time, comparing Linear, Algebraic, and Numeric models. 42

4.3 Free decay test for the sphere over time, comparing Linear, Algebraic, and Numeric models. . . . 42
4.4 Free decay test for the spline over time, comparing Linear, Algebraic, and Numeric models. . . . 43
4.5 Uncontrolled dynamic response of the cylinder across different wave periods. . . . 44
4.6 Uncontrolled dynamic response of the sphere across different wave periods. . . . 44
4.7 Uncontrolled dynamic response of the spline across different wave periods. . . . 45
4.8 Comparison of RAOs (Response Amplitude Operators) for the various geometries analysed. . . . 46
4.9 Trend in the optimal PTO damping coefficient ($B_{PTO,opt}$) as the wave period T varies for the three different geometries (Cylinder, Sphere, Spline). . . . 47
4.10 Kinematic response for the cylindrical geometry as a function of the wave period (T_w) under constant wave steepness: (left) maximum relative displacement and (right) maximum pitch angle. . . . 47
4.11 Absolute power extraction (left) and power ratio (right) as a function of the wave period T_w for the cylindrical geometry. . . . 48
4.12 Kinematic response for the spherical geometry under passive linear control as a function of the wave period (T_w). Maximum relative displacement (left) and maximum pitch angle (right). . . . 49
4.13 Absolute power extraction (left) and power ratio (right) for the Sphere geometry. 49
4.14 Kinematic response for the Spline geometry under passive control. . . . 50
4.15 Absolute power extraction (left) and corresponding linear overestimation ratio (right) for the Spline geometry under passive linear control. . . . 50
4.16 Comparison of the maximum pitch angle (left) and the relative displacement (rigth) across varying wave periods for the Linear and NLFK models. . . . 51
4.17 Kinematic response in heave (top) and pitch (bottom) for the cylindrical floater under reactive control, comparing Linear, Algebraic, and Numerical models. . . . 53
4.18 Relative heave displacement compared to the wave elevation for the cylindrical geometry. . . . 53
4.19 Instantaneous power extraction and mean power values under reactive control. . 54
4.20 Kinematic response in heave (top) and pitch (bottom) for the spherical floater under reactive control, comparing Linear, Algebraic, and Numerical models. . . . 55
4.21 Relative heave displacement for the spherical geometry. . . . 55
4.22 Instantaneous power extraction and mean power values under reactive control for the spherical geometry. . . . 56
4.23 Kinematic response in heave (top) and pitch (bottom) for the spline-based floater under reactive control, comparing Linear, Algebraic, and Numerical models. . . . 57
4.24 Relative heave displacement ($z - \eta$) compared to the wave elevation and the physical draft limit for the spline-based geometry. . . . 57
4.25 Instantaneous power extraction and mean power values under reactive control for the spline-based geometry, highlighting the differences between linear predictions and NLFK models. . . . 58

List of Tables

3.1 Main geometric and hydrostatic properties of the investigated axisymmetric floaters. For the Spline-based buoy, the defining geometrical coordinates represent the control nodes of the cubic Bézier curves. 27
3.2 Comparison of computation times for simulations of irregular waves over 1,000 iterations. 38

4.1 Wave periods and corresponding wave heights used in the simulations.Steepness($s = 0.018$). 40
4.2 Properties and mooring of the three geometries. 40
4.3 Comparison of the natural periods in Heave and Pitch for the three geometries. . 40
4.4 Reactive control parameters for the different geometries at $T_w = 8$ s, $H_w = 1.8$ m. 52
4.5 Comparison of computational times between NLFK solvers for the three analyzed geometries. 57

Chapter 1

Introduction

1.1 Context and Motivation

Due to ongoing global development and the worsening energy crisis, the limitations of conventional fossil fuels have become increasingly apparent. As the need to mitigate climate change accelerates the global transition to clean energy, the exploitation of offshore renewable resources has become a key and highly promising area of research. One renewable energy source that shows great potential and offers advantages in terms of energy density and predictability is ocean wave energy [3][4].
Unlike solar and wind power, which are by their very nature dependent on weather conditions and intermittent, technologies for harnessing ocean energy are attracting considerable interest thanks to their greater predictability and their ability to provide a more continuous energy supply [5].
Recent assessments indicate that ocean energy has enormous global potential; wave energy resources alone are estimated to amount to 29,500 TWh per year [6]. Exploiting even a fraction of this resource could lead to significant socio-economic and environmental benefits, ranging from grid stability to climate change mitigation, as illustrated in Figure 1.1. Wave energy converters

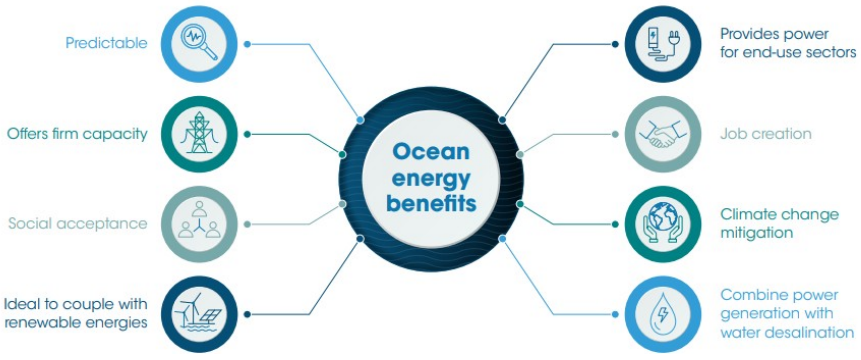


Figure 1.1: Benefits of ocean energy technologies.Adapted from IRENA and OEE (2023)

(WECs) are the technology used to convert the kinetic and potential energy of ocean waves into usable electrical energy. WECs are generally classified into three broad categories based on their operating principle and geometric orientation relative to the incident wave front: attenuators,

terminators and *point absorbers* [7].
A device is defined as a point absorber when its characteristic dimensions are considerably smaller than the wavelength of the incident wave. This specific configuration ensures considerable structural simplicity and the intrinsic ability to absorb the wave's energy regardless of its direction of propagation.The operating principle of the Point Absorber system, involves waves lifting the float; as it falls back down, the kinetic energy is captured and converted into electrical energy. These devices derive energy from the relative motion induced by waves between a moving body and a fixed or stationary structure,as schematically shown in Figure 1.2. The

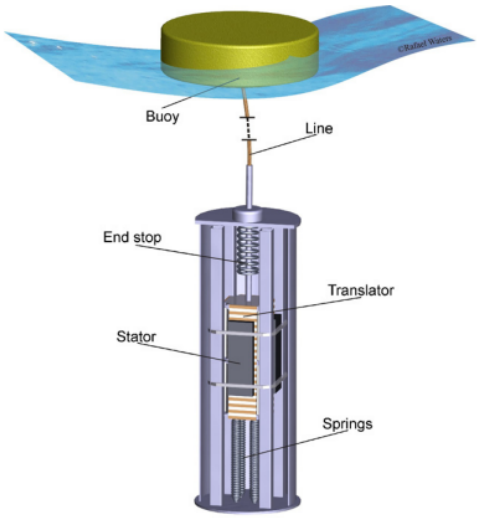


Figure 1.2: Schematic representation of the Swedish heaving buoy equipped with a direct-drive linear electrical generator. Source: Uppsala University, as cited in [1]

system that allow to capture the energy is the power take off (PTO). Depending on the physical principle employed, PTOs are primarily classified as hydraulic systems, mechanical transmissions, direct-drive linear generators or devices based on innovative materials. The commercial development of WECs still faces highly complex engineering challenges. Currently, [5] shows that the wave energy sector is still regarded as an immature sector, often described as lagging three decades behind wind energy, with an average technology readiness level (TRL) of around 6. One of the main obstacles to commercialisation is the lack of a standardised WEC device. The main obstacle to industrial-scale deployment lies in the high levelised cost of energy (LCoE) compared with other renewable sources. Added to this is the need to ensure the absolute durability of the devices and PTO systems under extreme marine conditions, which can generate high structural loads.
To make wave energy economically competitive, it is essential to maximise power extraction under normal operating conditions. This objective is typically achieved through the implementation of advanced control strategies. Such strategies intentionally force the device to exaggerate the amplitude of its movement in order to operate in resonance with the incident wave.[8]
Consequently, the accuracy of conventional numerical tools based on linear potential theory decreases rapidly. These linear models lead to significant discrepancies compared with experimental data. On the other hand, the use of fully non-linear Computational Fluid Dynamics (CFD) models is still highly impractical for large-scale applications in the field of wave energy;

CFD requires enormous computation times and is notoriously difficult when it comes to accurately propagating gravity waves over long periods. [9]
To bridge this gap between imprecise linear tools and computationally prohibitive CFD models, advanced hydrodynamic models focus on the most critical sources of non-linearity. Among these, the component that most significantly affects the accuracy of predicted energy output is the Froude-Krylov (FK) dynamic force. Unlike the classical linear approach, which evaluates the pressure on an average wetted surface assumed to be constant, a rigorous estimate requires an advanced numerical approach. In this hybrid methodology, the static and dynamic non-linear Froude-Krylov forces are calculated by integrating the pressure field over the exact instantaneous wetted surface of the converter, whilst the radiation and diffraction forces are treated as linear.
Overcoming the mathematical limitations of linear models by accurately and efficiently calculating these non-linear Froude–Krylov forces currently represents one of the most challenging tasks in WEC research.

1.2 Thesis objectives

The main objective of this thesis emerges as a natural response to a complex engineering challenge. As discussed, non-linear Froude-Krylov forces (NLFK) play a fundamental role when the buoy is subjected to the large kinematic excursions required to maximise efficiency. Under these operating conditions, using linear models leads to inaccurate estimates of power absorption and an incapability to predict critical phenomena ,such as pitch instability.
Consequently, an accurate and dynamic calculation of the FK forces is essential for selecting and optimising realistic control systems capable of predicting and exploiting the buoy's actual behaviour at sea. However, the joint optimisation of the PTO and the geometric design requires the evaluation of a large number of operational scenarios; a task that requires high computational costs.
To address this computational bottleneck, this research leverages and expands upon NLFK4ALL, an open-source mathematical toolbox [10]. This framework was specifically conceived to provide computationally efficient evaluations of non-linear Froude-Krylov forces, bridging the gap between inaccurate linear tools and extremely slow CFD models. Building upon this open-source foundation, the specific aims of this study are to:

- **Extend the mathematical framework** to support new and more complex axially symmetric geometries, specifically evaluating spherical profiles and novel shapes generated via cubic splines.
- **Implement and compare two distinct mathematical strategies** for calculating NLFK forces in 3 degrees of freedom (surge, heave, and pitch): an adaptive numerical method based on 2D Simpson's quadrature and a highly efficient closed-form algebraic solution.
- **Evaluate the trade-off between hydrodynamic accuracy and computational efficiency** through rigorous time-domain simulations under regular wave conditions.
- **Analyse the kinematic responses and power extraction capabilities** of the different geometries when coupled with passive and reactive PTO control strategies, highlighting critical non-linear effects that standard linear models fail to capture.

Chapter 2

Theoretical Framework

The hydrodynamic interaction between WECs and waves is a complex non-linear process which, under certain conditions, can be simplified. The non-linear dynamics of the WEC, taking into account reactive forces such as those in mooring systems or damper-spring systems for power take-off, are simplified using the principle of superposition, in which linear combinations of simple solutions can be used to obtain more complex solutions.

2.1 Potential Flow Theory

The modelling of wave-body interaction is based on an irrotational, incompressible and non-viscous flow that generates a velocity potential ($\phi(x, y, z, t)$) [11].
Taking into account the elevation of the free surface (η), these assumptions lead to a set of governing equations and boundary conditions that mathematically define the general potential flow problem. Considering, Δ the Laplace operator, ∇ the gradient operator, ∂ the partial operator, g the acceleration due to gravity, and M any point in the fluid domain,the equations are:

1. Laplace's equation
$$\Delta\phi = 0 \tag{2.1}$$

2. A kinematic free-surface boundary condition, evaluated on $z = \eta$, which ensures that no material flux occurs across the free-surface
$$\frac{\partial\eta}{\partial t} - \frac{\partial\phi}{\partial z} + \nabla\phi \cdot \nabla\eta = 0 \tag{2.2}$$

3. A dynamic free-surface boundary condition
$$g\eta + \frac{\partial\phi}{\partial t} + \frac{1}{2}|\nabla\phi|^2 = 0 \tag{2.3}$$

4. Impermeability condition on the seabed.
$$\frac{\partial\phi}{\partial n} = 0 \tag{2.4}$$

5. Impermeability condition for a body moving at a velocity V, with a normal n, on the wetted surface of the body.
$$\frac{\partial \phi}{\partial n}(M,t) = V \cdot n(M,t) \tag{2.5}$$

6. A radiation condition, where the total potential ϕ is equal to the sum of an incident potential ϕ_0 and a perturbed potential ϕ_p

$$\phi = \phi_0 + \phi_p \tag{2.6}$$

The equations above are non-linear due to the presence of second-order terms. However, the problem can be solved using *linear theory*, based on the assumption that the wavelength is much greater than the wave amplitude. Consequently, the second-order terms can be neglected as their magnitude is much smaller than that of the other linear terms.
With the adoption of linear theory, the boundary conditions are no longer applied to the instantaneous wave elevation but they are only considered at the equilibrium position of the free water surface ($z = 0$).
By considering infinitesimal wave amplitudes the linearised mean surface boundary condition can be written as:
$$\frac{\partial^2 \phi}{\partial t^2} + g\frac{\partial \phi}{\partial z} = 0 \tag{2.7}$$
The Eq.2.7 can be solved for a given frequency of the incident wave, enabling a solution to be obtained for more complex sea conditions using the principle of superposition. Since the individual frequencies can be treated independently, the velocity potential can be expressed in the complex domain as:
$$\Phi = \Re\{\phi(x,y,z)e^{-i\omega t}\} \tag{2.8}$$
where i is the complex unit and ω the angular frequency.
This mathematical formulation forms the basis for linear frequency-domain models based on analytical methods, the boundary element method (BEM) and the finite element method (FEM), which are used to evaluate the performance of WECs. In practice, open-source BEM software such as NEMOH uses precisely this theoretical basis to derive the linear hydrodynamic coefficients of the device (added mass, radiation damping and excitation forces).

2.2 Hydrodynamics Model of the Floating Body

The interaction between a body and an incident wave, under the assumptions of a non-viscous, irrotational and incompressible fluid, is described by Newton's second law as follows:

$$m\ddot{\xi}(t) = F_g - \iint_{S(t)} P(t) n dS + F_{PTO}(t) \tag{2.9}$$

The Eq. 2.9 is defined by taking a reference frame at its centre of gravity and a general displacement vector $\xi = (x, y, z)$. The other paramenter involved in the Newton's second law are:

- m; mass of the body
- F_g; gravity force
- S; the sumbmerged surface

- P; the pressure
- n; the vector normal to the surface
- $F_{PTO}(t)$; the power take-off force.

The pressure $P(t)$ acting on the body can be derived from the incident flow applying Bernoulli's equation [12]:

$$P(t) = -\rho g z(t) - \rho \frac{\partial \phi(t)}{\partial t} - \rho \frac{|\nabla \phi(t)|^2}{2} \tag{2.10}$$

where ρ is the density of water, g is the acceleration due to gravity, $P_{st} = -\rho g z$ is the hydrostatic pressure and ϕ is the flow potential, which can be expressed as the sum of the unperturbed incident flow potential ϕ_I, the diffraction potential ϕ_D and the radiation potential ϕ_R:

$$\phi(t) = \phi_I + \phi_D + \phi_R \tag{2.11}$$

The Eqs. 2.9,2.10,2.11 lead to define different forces:

◇ $F_{FK_{st}}$ is the static Froude–Krylov force; It is related to the variation in the submerged volume generates a net force allowing to return the buoy to its original resting state.It is derived from the balance between the force of gravity and Archimedes' force.

$$\mathbf{F}_{FK_{st}}(t) = \mathbf{F}_g - \iint_{S(t)} P_{st}(t)\mathbf{n}\,\mathrm{d}S \tag{2.12}$$

◇ $F_{FK_{dy}}$ is the dynamic Froude-Krylov force

$$\mathbf{F}_{FK_{dy}}(t) = -\iint_{S(t)} P_{dy}(t)\mathbf{n}\,\mathrm{d}S \tag{2.13}$$

where $P_{dy} = -\rho\frac{\partial \phi_I}{\partial t} - \rho\frac{|\nabla \phi_I|^2}{2}$ the dynamic pressure.

◇ F_D is the diffraction force

$$\mathbf{F}_D(t) = -\iint_{S(t)} P_D(t)\mathbf{n}\,\mathrm{d}S \tag{2.14}$$

where $P_D = -\rho\frac{\partial \phi_D}{\partial t} - \rho\frac{|\nabla \phi_D|^2}{2}$ the diffraction pressure.

◇ F_R is the radiation force. This component arises from the oscillation of the device. As the point absorber moves, it displaces the surrounding fluid and generates new outgoing waves. This fluid resistance opposes the body's motion and is mathematically decomposed into two parts: an *added mass* term (proportional to the body's acceleration) and a *radiation damping* term (proportional to its velocity, representing the energy radiated away).

$$\mathbf{F}_R(t) = -\iint_{S(t)} P_R(t)\mathbf{n}\,\mathrm{d}S \tag{2.15}$$

where $P_R = -\rho\frac{\partial \phi_R}{\partial t} - \rho\frac{|\nabla \phi_R|^2}{2}$ the diffraction pressure.

Consequently the Eq.2.9 is rewritten as:

$$m\ddot{\boldsymbol{\xi}} = \mathbf{F}_{FK_{st}} + \mathbf{F}_{FK_{dy}} + \mathbf{F}_D + \mathbf{F}_R + \mathbf{F}_{PTO} \tag{2.16}$$

In order to explicitly evaluate both the static and dynamic Froude–Krylov forces, it is necessary to define the total pressure field $p(x, z, t)$ acting on the wetted surface. Assuming the linear wave theory (Airy wave theory) for small-amplitude waves, the non-linear term proportional to the square of the fluid velocity, $\frac{|\nabla\phi_I|^2}{2}$, in Bernoulli's equation is considered negligible [13]. Consequently, the total pressure is decomposed into a hydrostatic component (p_{st}) and a linear dynamic component (p_{dy}). By substituting the velocity potential of a regular travelling wave into the linearised Bernoulli equation. The total pressure, as shown by [8], is::

$$p(x, z, t) = p_{st} + p_{dy} = -\rho g z + \rho g a \cos(\omega t - kx)\frac{\cosh(k(z + h))}{\cosh(kh)} \tag{2.17}$$

where a is the wave amplitude, ω is the angular frequency of the wave, k is the wave number and h is the water depth.

2.3 Linear Froude-Krylov Forces

As established in the Sect.2.1,the linear approach assumes that the wave has a small amplitude and low steepness; therefore, the potential problem is linearised and solved around the hydrostatic equilibrium position of the device. Under this assumption, the constant mean wetted area (S_M) is used to calculate the forces. The equation of motion for the system is consequently simplified:

$$m\ddot{\xi} = \underbrace{-K_H\xi}_{F_{FK_{st}}} \underbrace{- \int_{-\infty}^{\infty} K_{ex}(t-\tau)\eta(\tau)d\tau}_{F_{ex}=F_{FK_{dy}}+F_D} \underbrace{- \mu_\infty\ddot{\xi} - \int_{-\infty}^{\infty} K_R(t-\tau)\dot{\xi}(\tau)d\tau}_{F_R} + F_{PTO} \tag{2.18}$$

In this fully linear model:

- The static Froude-Krylov force ($F_{FK_{st}}$) is described by the linear hydrostatic stiffness K_H multiplied by the displacement ξ.
- The total excitation force (F_{ex}), representing the sum of the dynamic Froude-Krylov and diffraction forces, is computed via the convolution product between the excitation impulse-response function (IRF) K_{ex} and the free-surface elevation η.
- The radiation force (F_R) relies on the added mass at infinite frequency μ_∞ and the radiation IRF K_R, according to Cummins' equation [14].

These linear hydrodynamic coefficients and impulse response functions must be pre-calculated. They are extracted using the open-source BEM software **NEMOH**.
Although linearisation offers clear computational advantages, it becomes highly inaccurate when the WEC undergoes large-amplitude movements. To maximise energy harvesting, modern control strategies push the WEC beyond the simple behaviour of a *wave follower*, inducing large excursions that drastically alter the effective submerged area.
To accurately capture these dynamics, the implemented NLFK4ALL model adopts a hybrid (or *body-exact*) approach. Radiation and diffraction forces are kept linear, as the non-linear effects

on these components are considered secondary, and their coefficients continue to be provided by NEMOH
In contrast, the model does not take the mean wetted area S_M into account when calculating the Froude–Krylov forces (both static and dynamic) in a strictly non-linear manner. The equations $F_{FK_{st}}$ and $F_{FK_{dy}}$ are solved by integrating the fluid pressure over the exact instantaneous wetted surface $S(t)$ of the moving body.

2.4 Linear Frequency-Domain

The hydrodynamic modelling of a WEC, governed in the time domain by the equations described in the Sec. 2.2 , can also be approached in the frequency domain. Based on the assumption of a linear system with small-amplitude float movements, this approach evaluates the device's response to individual harmonic oscillations. This allows the behaviour of the WEC to be predicted rapidly and with high computational stability through the principle of superposition. [15] shows the equation of motion in the frequency domain is:

$$-\omega^2 m\hat{\xi}(\omega) = \hat{F}_{ex}(\omega) + \hat{F}_R(\omega) - K_H\hat{\xi}(\omega) \tag{2.19}$$

where m is the mass of the body, $\hat{\xi}(\omega)$ is the complex displacement amplitude, and on the right-hand side::

- $\hat{F}_{ex}(\omega)$ is the *excitation force* (complex amplitude), comprising both the dynamic Froude-Krylov force and the diffraction force.
- $\hat{F}_R(\omega)$ is the *radiation force*, which decomposes into a frequency-dependent added mass term $A(\omega)$ and a radiation damping term $B(\omega)$. Mathematically, it is expressed as $\hat{F}_R(\omega) = -(-\omega^2 A(\omega) + i\omega B(\omega))\hat{\xi}(\omega)$.
- $-K_H\hat{\xi}(\omega)$ represents the *hydrostatic restoring force*.

The Response Amplitude Operator (RAO)

This frequency-domain formulation leads to the definition of the Response Amplitude Operator (RAO), a complex transfer function that determines the effect of a specific sea state on the buoy. By substituting the force components into the equation of motion, the RAO for a generic degree of freedom can be calculated as:

$$RAO(\omega) = \frac{\hat{\xi}(\omega)}{\hat{\eta}(\omega)} = \frac{F_e(\omega)}{K - \omega^2(M + M_a(\omega)) + j\omega B(\omega)} \tag{2.20}$$

The magnitude of the RAO indicates the amplification of the device's motion relative to the incident wave amplitude, while its phase determines the lag between the wave elevation and the WEC's response.

2.5 The NLFK4ALL Mathematical Framework

To accurately and efficiently calculate the exact non-linear Froude-Krylov (NLFK) forces on the instantaneous wetted surface of the WEC, this study adopts the mathematical framework provided by the open-source **NLFK4ALL** toolbox. The basic idea behind this methodology is to find an optimal compromise between high-fidelity mathematical modelling and reduced computation times, an essential requirement for in-depth parametric studies and model-based control

optimisation. Rather than relying on slow mesh-based approaches, which require computationally expensive remeshing routines at every time step, this method exploits the axisymmetric nature of point absorbers to represent the wetted surface analytically.

2.5.1 Reference Frames in 3-DoF configuration

A distinctive feature of the toolbox is the interaction between two reference frames: a global reference frame known as the World-Frame (WF) and a non-inertial local reference frame known as the Body-Fixed Frame (BF). The WF is characterised by the coordinates (x, y, z), whilst the BF is characterised by $(\hat{x}, \hat{y}, \hat{z})$. The origin of the local system is fixed at the reference point (RefP) of the float. Both reference systems are illustrated in Fig. 2.1. Using cylindrical

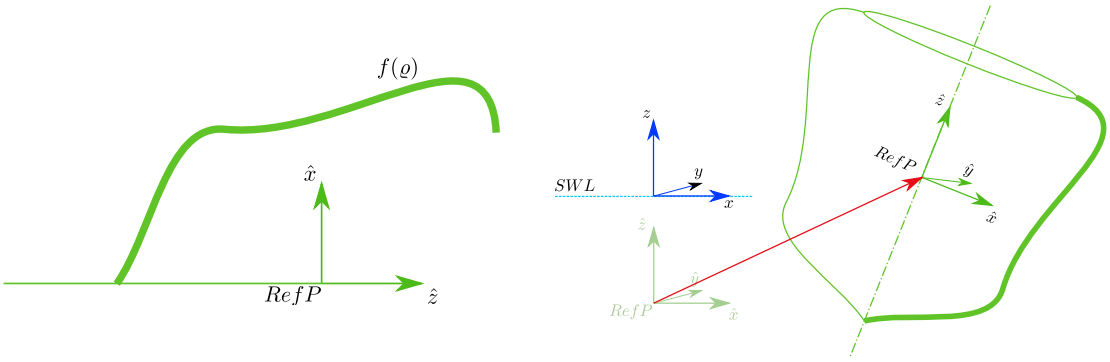


Figure 2.1: Generic profile of revolution in the BF (left); relative position between frames after displacement (right).

coordinates, the axisymmetric geometry is defined by the revolution of a generic function $f(\varrho)$, between ϱ_1 and ϱ_2.
Hence, the parameterisation of the axisymmetric geometry in BF is set out in Eq. (2.21)

$$\begin{cases} \hat{x}(\varrho, \vartheta) = f(\varrho)\cos\vartheta \\ \hat{y}(\varrho, \vartheta) = f(\varrho)\sin\vartheta \\ \hat{z}(\varrho, \vartheta) = \varrho \end{cases} \quad , \quad \vartheta \in [-\pi, \pi) \wedge \varrho \in [\varrho_1, \varrho_2] \tag{2.21}$$

The scenario described involves simulating an axially symmetric buoy in 3 DoF, specifically surge (x_R) , heave (y_R) and pitch (θ).The translation vector C, which describes the instantaneous position of the RefP in the World-Frame, reduces to:

$$C = \begin{pmatrix} x_R \\ 0 \\ z_R + z_{RefP} \end{pmatrix} \tag{2.22}$$

Taking Euler rotation sequences into account, restricting them to rotations about the $\hat{y}$-axis only, and extending the Cartesian plane to $\mathbb{R}^4$, the resulting rotation-translation matrix is as follows:

$$R = \begin{bmatrix} c\theta & 0 & s\theta & x_R \\ 0 & 1 & 0 & 0 \\ -s\theta & 0 & c\theta & z_R + z_{RefP} \\ 0 & 0 & 0 & 1 \end{bmatrix} \tag{2.23}$$

The spatial mapping of any generic point from the non-inertial body coordinates onto the global inertial system is expressed through the relation:

$$\begin{pmatrix} x \\ y \\ z \\ 1 \end{pmatrix} = R \begin{pmatrix} \hat{x} \\ \hat{y} \\ \hat{z} \\ 1 \end{pmatrix} \tag{2.24}$$

A conic section, expressed in cylindrical coordinates, characterised by a profile of revolution $f(\varrho) = m\varrho + q$, and using the Eq. 2.24, can be expressed as:

$$\begin{cases} x = (m\varrho + q)\cos\vartheta c\theta + \varrho s\theta + x_R \\ y = (m\varrho + q)\sin\vartheta \\ z = -(m\varrho + q)\cos\vartheta s\theta + \varrho c\theta + z_R + z_{RefP} \end{cases} \tag{2.25}$$

where $c\theta$ and $s\theta$ are the components of the Euler rotation matrix and represent the cosine and sine of θ respectively. The elements of the transformation matrix R (Eq.2.23) will henceforth be denoted using the standard index notation R_{ij} (where i and j represent the row and column, respectively). Using this compact notation, the three equations can be rewritten in a more generalised and manageable form:

$$\begin{cases} x = R_{11}(m\varrho + q)\cos\vartheta + R_{13}\varrho + R_{14} \\ y = (m\varrho + q)\sin\vartheta \\ z = R_{31}(m\varrho + q)\cos\vartheta + R_{33}\varrho + R_{34} \end{cases} \tag{2.26}$$

2.5.2 Intersection and Integration limits

The toolbox exploit the analytical representation of the intersection between the body surface and the free surface elevation (η). In a general scenario, a two-dimensional wave within the World-Frame (WF) is defined as a function of the spatial coordinate x and time t. To model an irregular sea state, it is typically represented as a superposition of multiple harmonic components:

$$\eta(x,t) = \sum_{i=1}^{N_\omega} a_i \cos(\omega_i t + \varphi_i - k_i x) \tag{2.27}$$

where a_i, ω_i, φ_i, and k_i denote the amplitude, angular frequency, phase, and wave number of the i-th wave component, respectively. A monochromatic regular wave naturally emerges as the limiting case when $N_\omega = 1$. Since the subsequent geometric analyses are evaluated at a fixed time instant $t = t_0$, the explicit time dependence of the free-surface elevation η will be omitted. As investigated by [16], it is convenient to define the NLFK integrals in the BF, hence requiring a mapping of the free surface elevation from the WF onto the BF ($\hat{\eta}$). The representation of the surface wave in 4D and in WF is:

$$\Gamma = \begin{pmatrix} x \\ y \\ \eta(x) \\ 1 \end{pmatrix} \tag{2.28}$$

Taking Eq. 2.24 into account, the wave surface in BF is as follows:

$$\hat{\Gamma} = R^{-1}\Gamma \tag{2.29}$$

To determine the point of intersection, the third line of equation 2.29 must be equal to ϱ, giving:

$$\varrho = (0,0,1,0)R^{-1}\begin{pmatrix}(1,0,0,0)R(f(\varrho)\cos\vartheta, f(\varrho)\sin\vartheta, \varrho, 1)'\\(0,1,0,0)R(f(\varrho)\cos\vartheta, f(\varrho)\sin\vartheta, \varrho, 1)'\\\eta\left((1,0,0,0)R(f(\varrho)\cos\vartheta, f(\varrho)\sin\vartheta, \varrho, 1)'\right)\\1\end{pmatrix} \tag{2.30}$$

By exploiting the properties of the matrix R, the Eq. 2.30 becomes:

$$\begin{aligned}&f(\varrho)\left(\cos\vartheta(R_{11}R_{13}+R_{21}R_{23})+\sin\vartheta(R_{12}R_{13}+R_{22}R_{23})\right)+\\&\varrho(R_{13}^2+R_{23}^2-1)+R_{33}(\eta(\vartheta,\varrho)-C(3)))=0\end{aligned} \tag{2.31}$$

A reasonable approximation, given that the waves are not very steep, is to use the *flat approximation*, i.e. to assume that the slope of the wave across the buoy's diameter is negligible, allowing the free surface immediately surrounding the device to be treated as a perfectly horizontal plane. The elevation of this plane is defined as constant and equal to the instantaneous wave elevation evaluated exactly at the buoy's central vertical axis, yielding $\eta \approx \eta(x_R, t)$. By

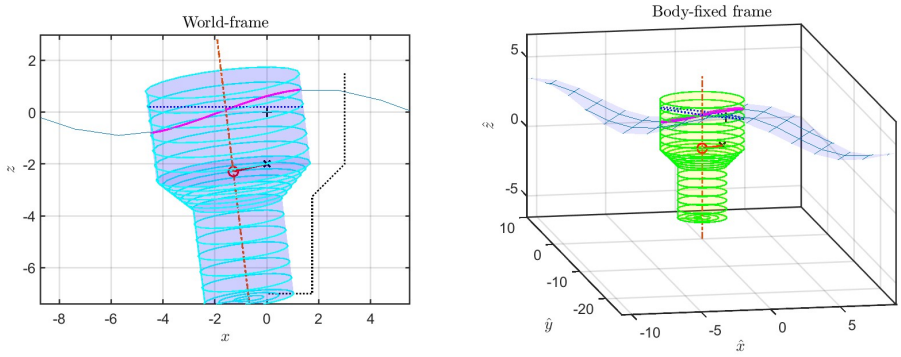


Figure 2.2: Plot of the flat approximation of the free-surface elevation (blue dotted line) and the exact representation (purple) in WF and BF.

defining the integration limits for a cone expressed in the local reference frame (BF), the lower limit depends exclusively on the fixed geometry of the body (or the specific patch) and therefore remains constant. The upper limit, by contrast, varies instantaneously as it corresponds to the intersection with the free surface of the fluid. Referring to Eq. 2.31 and applying the flat-surface approximation in a 3 DoF configuration, the upper limit of integration is given by:

$$\varrho_2(\vartheta) = \frac{\eta - R_{34} - R_{31}q\cos\vartheta}{R_{33} + R_{31}m\cos\vartheta} \tag{2.32}$$

The Eq. 2.32 can be solved algebraically if it is assumed that the pitch rotation angles are small enough that the cosine terms can be neglected.

2.5.3 Integration

The geometry of the float is described in the BF, defined by the $(\hat{x}, \hat{y}, \hat{z}) \in \mathbb{R}^3$. It is possible to parameterise it using cylindrical or polar coordinates, thus moving on to (u, v). Considering the integral of a generic function, it is important, in the mapping, to define and include the unit vectors of the directions u and v.

$$I = \iint_S g(\hat{x}, \hat{y}, \hat{z}) dS \tag{2.33}$$

$$I = \int_u \int_v g(u, v) \|\mathbf{e}_u \times \mathbf{e}_v\| \, du \, dv \tag{2.34}$$

$$\mathbf{e}_u = \begin{pmatrix} \frac{\partial \hat{x}}{\partial u} \\ \\ \frac{\partial \hat{y}}{\partial u} \\ \\ \frac{\partial \hat{z}}{\partial u} \end{pmatrix} \tag{2.35}$$

$$\mathbf{e}_v = \begin{pmatrix} \frac{\partial \hat{x}}{\partial v} \\ \\ \frac{\partial \hat{y}}{\partial v} \\ \\ \frac{\partial \hat{z}}{\partial v} \end{pmatrix} \tag{2.36}$$

2.5.4 Analytical Parameterisation

Depending on the geometry of the solid in question, it may be possible to parameterise it using cylindrical or polar coordinates

Cylindrical Coordinates

$$\begin{cases} \hat{x}(\varrho, \vartheta) = f(\varrho) \cos \vartheta \\ \hat{y}(\varrho, \vartheta) = f(\varrho) \sin \vartheta \\ \hat{z}(\varrho, \vartheta) = \varrho \end{cases} \quad , \quad \vartheta \in [-\pi, \pi) \wedge \varrho \in [\varrho_1, \varrho_2] \tag{2.37}$$

$$\mathbf{e}_\varrho = \begin{pmatrix} f(\varrho)' \cos \vartheta \\ f(\varrho)' \sin \vartheta \\ 1 \end{pmatrix} \tag{2.38}$$

$$\mathbf{e}_\vartheta = \begin{pmatrix} -f(\varrho) \sin \vartheta \\ f(\varrho) \cos \vartheta \\ 0 \end{pmatrix} \tag{2.39}$$

$$\mathbf{e}_\varrho \times \mathbf{e}_\vartheta = f(\varrho) \begin{pmatrix} -\cos \vartheta \\ -\sin \vartheta \\ f(\varrho)' \end{pmatrix} \tag{2.40}$$

$$\|\mathbf{e}_\varrho \times \mathbf{e}_\vartheta\| = f(\varrho) \sqrt{1 + f(\varrho)'^2} \tag{2.41}$$

The inward-pointing unit normal vector to the surface can be computed as:

$$\mathbf{n} = \frac{\mathbf{e}_\varrho \times \mathbf{e}_\vartheta}{\|\mathbf{e}_\varrho \times \mathbf{e}_\vartheta\|} = \frac{1}{\cancel{f(\varrho)}\sqrt{1+f(\varrho)'^2}}\cancel{f(\varrho)}\begin{pmatrix}-\cos\vartheta\\-\sin\vartheta\\f(\varrho)'\end{pmatrix} = \frac{1}{\sqrt{1+f(\varrho)'^2}}\begin{pmatrix}-\cos\vartheta\\-\sin\vartheta\\f(\varrho)'\end{pmatrix} \tag{2.42}$$

Finally achieving:

$$\iint_S \mathbf{n} dS = \int_\vartheta \int_\varrho \cancel{\|\mathbf{e}_\varrho \times \mathbf{e}_\vartheta\|}\frac{\mathbf{e}_\varrho \times \mathbf{e}_\vartheta}{\cancel{\|\mathbf{e}_\varrho \times \mathbf{e}_\vartheta\|}} d\varrho\, d\vartheta \tag{2.43}$$

2.5.5 Normalization of the integration domain

During the numerical integration of forces, the model normalises the integration domain. This means that, with cylindrical coordinates defined as $\vartheta \in [-\pi, \pi) \wedge \varrho \in [\varrho_1, \varrho_2]$, it is more convenient to have a domain of the form: $\vartheta \in [-\pi, \pi) \wedge \tilde{\varrho} \in [0, 1]$. Eqs. 2.44 - 2.45 are the final result of the normalization

$$\tilde{\varrho} = \varrho_1 + \varrho\,(\varrho_2(\vartheta) - \varrho_1) \tag{2.44}$$

$$\iint_S \mathbf{n} dS = \int_{-\pi}^{\pi}\int_{\varrho_1}^{\varrho_2} (\mathbf{e}_\varrho(\varrho,\vartheta) \times \mathbf{e}_\vartheta(\varrho,\vartheta))\; d\varrho\, d\vartheta = \int_{-\pi}^{\pi}\int_{0}^{1} (\mathbf{e}_\varrho(\tilde{\varrho},\vartheta) \times \mathbf{e}_\vartheta(\tilde{\varrho},\vartheta))\,(\varrho_2(\vartheta) - \varrho_1)\; d\tilde{\varrho}\, d\vartheta \tag{2.45}$$

2.5.6 Geometric Properties Evaluation

To validate the numerical framework, the toolbox computes fundamental geometric properties—namely the surface area, volume, and centre of buoyancy—using analytical surface integrations. The general formulation assumes an axisymmetric body comprising a lateral surface bounded by top and bottom horizontal discs.

Surface Area and Volume

The total surface S is the sum of the lateral boundary (S_L) and the upper and lower discs. While the bases are evaluated as standard circular areas (e.g., πR_1^2 for a bottom radius $R_1 = f(\varrho_1)$), the lateral area is computed by integrating the generic radial profile $f(\varrho)$ over the azimuthal (ϑ) and vertical (ϱ) coordinates:

$$S_L = \int_{-\pi}^{\pi}\int_{\varrho_1}^{\varrho_2} f(\varrho)\sqrt{1+[f'(\varrho)]^2}\; d\varrho\, d\vartheta \tag{2.46}$$

Similarly, the total enclosed volume V can be evaluated by integrating the normal vector components over the bounding surfaces. By projecting this integration along the $\hat{z}$-axis, the volume is efficiently derived by summing the separate geometric contributions of the lateral profile and the flat extremities.

Centre of Buoyancy

The integration domain to compute the center of buoyancy is strictly limited to the submerged portion of the device, bounded between the bottom coordinate ϱ_1 and the still water level ϱ_0. Due to the rotational symmetry of the body, follows that $\hat{x}_B = \hat{y}_B = 0$. The exact vertical position $\hat{z}_B$ is thus calculated as a surface integral scaled by the displaced volume V:

$$\hat{z}_B = -\frac{1}{2V}\left(\int_{-\pi}^{\pi}\int_{\varrho_1}^{\varrho_0} \varrho^2 f(\varrho) f'(\varrho)\ d\varrho\ d\vartheta + \pi R_1^2 \varrho_1^2 - \pi R_0^2 \varrho_0^2\right) \tag{2.47}$$

where $R_0 = f(\varrho_0)$ represents the instantaneous radius of the body evaluated at the free surface intersection.

2.5.7 Nonlinear Froude-Krylov Forces

The mathematical framework set out in sections 2.5.1;2.5.2;2.5.3 enables the definition of non-linear Froude-Krylov forces, using a numerical integration based on Simpson's method, which allows the simulation to be extended to 6 DoF and the force to be calculated algebraically, but limited to 3 DoF. Assuming a 3-DoF configuration (surge, heave, and pitch) and applying the Wheeler stretching method to Airy's linear wave theory [8],from the Eq. 2.17 the pressure field mapped onto the Body-Fixed (BF) reference frame is defined as:

$$p_{st,BF} = \rho_w g \cdot (\hat{x} \cdot R_{31} + \hat{z} R_{33} + R_{34}) \tag{2.48}$$

$$p_{dy,BF} = \rho_w g a \cos\left(\omega t - k \cdot [\hat{x} \cdot R_{11} + \hat{z} \cdot R_{13} + R_{14}]\right) \cdot e^{k(\hat{x} \cdot R_{31} + \hat{z} R_{33} + R_{34} - \bar{\eta})} \tag{2.49}$$

where:

- $p_{st,BF}$: Static pressure computed in the body-fixed reference frame.
- $p_{dy,BF}$: Dynamic pressure computed in the body-fixed reference frame.
- ρ_w : Sea water density.
- g: Acceleration of gravity.
- $\hat{x}$, $\hat{z}$: Local coordinates of the point on the body surface where the pressure is evaluated. .
- R_{11}, R_{13}, R_{14}, R_{31}, R_{33}, R_{34}: Individual elements of the homogeneous transformation matrix R, identified by their row and column indices. (Sec. 2.5.1)
- a: Incident wave amplitude.
- ω: Wave angular frequency, equal to $\frac{2\pi}{T}$ (where T is the wave period).
- t: Time.
- k: Wave number, equal to $\frac{2\pi}{\lambda}$ (where λ is the wavelength).
- $\bar{\eta}$: Free surface elevation approximated as a horizontal plane evaluated at the central vertical axis of the floater (*Flat Approximation*).

The static and dynamic FK forces are defines as:

$$\mathbf{F}_{FK_{st}} = \mathbf{F}_g + \iint\limits_{S(t)} p_{st}\mathbf{n}\ dS \tag{2.50}$$

$$\mathbf{F}_{FK_{dy}} = \iint\limits_{S(t)} p_{dy}\mathbf{n}\ dS \tag{2.51}$$

the term $\mathbf{F}_g = (0, 0, -mg)'$ is the gravity force, with m the mass of the body, $S(t)$ the instantaneous wetted surface, and $\mathbf{n}$ the unity vector normal to the surface.
As regards static and dynamic FK moments, if the generic position vector is denoted by $\mathbf{r}$ and the position vector of the centre of gravity s is denoted by $\mathbf{r}_g$, it follows that:

$$\mathbf{T}_{FK_{st}} = \mathbf{r}_g \times \mathbf{F}_g + \iint\limits_{S_w} p_{st}\,(\mathbf{r} \times \mathbf{n})\ dS \tag{2.52}$$

$$\mathbf{T}_{FK_{dy}} = \iint\limits_{S_w} p_{dy}\,(\mathbf{r} \times \mathbf{n})\ dS \tag{2.53}$$

where, in cylindrical coordinates:

$$\mathbf{r} = \begin{cases} \hat{x}(\varrho, \vartheta) = f(\varrho)\cos\vartheta \\ \hat{y}(\varrho, \vartheta) = f(\varrho)\sin\vartheta \\ \hat{z}(\varrho, \vartheta) = \varrho \end{cases} \quad , \quad \vartheta \in [-\pi, \pi) \wedge \varrho \in [\varrho_1, \varrho_2] \tag{2.54}$$

$$\mathbf{n}dS = \mathbf{e}_\varrho \times \mathbf{e}_\vartheta = f(\varrho) \begin{pmatrix} -\cos\vartheta \\ -\sin\vartheta \\ f(\varrho)' \end{pmatrix} \tag{2.55}$$

$$(\mathbf{r} \times \mathbf{n})\, dS = \mathbf{r} \times (\mathbf{e}_\varrho \times \mathbf{e}_\vartheta) = \begin{pmatrix} f(\varrho)\sin\vartheta\,(f(\varrho)f(\varrho)' + \varrho) \\ -f(\varrho)\cos\vartheta\,(f(\varrho)f(\varrho)' + \varrho) \\ 0 \end{pmatrix} \tag{2.56}$$

2.6 Numerical Integration via 2D Simpson's Rule

When the WEC undergoes multi-degree-of-freedom motions, including significant pitch and roll rotations,it is not possible to obtain closed algebraic solutions. Consequently, to maintain a fully coupled 6-DoF operational space, the nonlinear Froude-Krylov integrals must be evaluated using a numerical approach. To optimize the numerical process, the mathematical framework avoids calculating the integrals in the global World-Frame (WF). Once the pressure field is mapped onto BF, the resulting surface integrals are evaluated via a 2D-quadrature scheme. Specifically, the NLFK4ALL toolbox implements a custom two-dimensional Simpson's rule algorithm, fundamentally based on the numerical quadrature techniques detailed by [17]. Although the adaptive integration functions included as standard (such as MATLAB's `integral2`) are extremely flexible and capable of handling 'unusual' integrands or severe singularities (for example, spherical regions near discontinuity boundaries), they involve complex processing of the input data and introduce a significant computational overhead. In contrast, the implemented two-dimensional Simpson's rule evaluates the integrand over a normalised rectangular domain (Eq.2.45) using pre-calculated evaluation matrices. For standard axially symmetric components, such as conical and cylindrical patches, this Simpson integration scheme proves to be highly numerically

stable, whilst drastically reducing computation time, making the model sufficiently efficient for dynamic simulations in the time domain.

2.7 Closed-Form Algebraic Solutions

An analysis of the equations governing the kinematics and dynamics of the float in the three degrees of freedom under consideration (surge, heave and pitch) reveals that the mapping of the free surface from the global reference frame (World-Frame) to the local reference frame (Body-Fixed frame) introduces trigonometric terms into the denominator of the upper limit of integration (Eq. 2.32).
Consequently, to solve the integral algebraically, it is necessary to introduce an approximation for small pitch angles ($\theta \approx 0$), which consists of assuming that the off-diagonal terms R_{13} and R_{31} of the rotation matrix are zero.
The impact and limitations of this assumption, highlighted by [16], depend on the geometric profile of the body: In the case of a cylindrical geometry, the assumption entails no loss of accuracy: the constant radius causes the trigonometric term to vanish naturally from the denominator, making the algebraic solution a perfect approximation of the exact numerical integration for any pitch angle. Conversely, for conical geometries, the slope of the profile causes the accuracy of the algebraic solution to decrease gradually as the pitch angle increases.
When adopting an algebraic approach, the challenge lies in formulating the dynamic pressure, the mathematical expression of which is characterised by the product of an exponential decay term and a spatial cosine function. Since this integral does not admit a closed-form solution using elementary functions, two distinct methods may be employed:

a) The Maclaurin series expansion of the spatial cosine term, in line with the approach initially adopted by [16].

b) Jacobi–Anger expansion → Bessel function→ Maclaurin.

However, as the approaches presented are algebraically equivalent, the decision to adopt strategy b) in this project is based solely on greater clarity and ease of code implementation, thereby avoiding errors when handling long trigonometric formulas. Finally, having reduced the problem to Bessel functions opens the way for future developments: by utilising the native functions already implemented in MATLAB packages for their evaluation, research can explore dedicated numerical algorithms, which may be even more efficient and stable than the current Simpson's quadrature. By applying the Jacobi–Anger expansion theorem, the incident plane wave is decomposed into a series of cylindrical harmonics, physically described by Bessel functions of the first kind, $J_n(z)$.
In this 3-degree-of-freedom configuration, the vertical dynamic force (heave) is governed entirely by the zero-order axisymmetric harmonic (J_0), whilst the asymmetric forces responsible for horizontal translation (surge) and the torque (pitch) are governed exclusively by the first-order harmonic (J_1). All higher-order harmonics ($n \geq 2$) cancel out analytically over the entire azimuthal integration domain. A detailed analytical derivation for solving these integrals, complete with explicit algebraic solutions for all the elementary geometries considered, is provided in the Appendix A.

2.8 Irregular Sea States

Real-world ocean environments are characterised by complex and irregular sea conditions. These conditions are modelled mathematically as a stochastic superposition of several linear wave

components, each defined by its own amplitude, frequency and random phase.
To describe analytically the energy distribution of these sea states at different frequencies, variance density spectra are used, such as the JONSWAP spectrum. This is derived from the fully developed Pierson-Moskowitz marine spectrum, with its energy peak amplified to account for wave generation limited by fetch.
The spectral density $S(f)$ is parameterised in terms of the significant wave height H_s, the peak frequency f_p (where $f_p = 1/T_p$) and the peak amplification factor γ :

$$S(f) = \alpha^* H_s^2 f_p^4 f^{-5} \exp\left[-\frac{5}{4}\left(\frac{f_p}{f}\right)^4\right] \gamma^{\exp\left[-\frac{(f-f_p)^2}{2\sigma^2 f_p^2}\right]} \tag{2.57}$$

where σ is the spectral width parameter, defined as:

$$\sigma = \begin{cases} 0.07 & \text{for } f \leq f_p \\ 0.09 & \text{for } f > f_p \end{cases} \tag{2.58}$$

The term α^* acts as a numerical normalization coefficient.Since the peak factor γ alters the total energy of the spectrum, α^* mathematically forces the curve to scale up or down, ensuring that the total energy of the simulated sea exactly matches the required wave height H_s.
To move from the frequency domain to a numerical simulation in the time domain, the continuous spectral density curve must be discretised into a finite number of harmonic components. By dividing the frequency range into narrow intervals of width Δf_i, the deterministic amplitude of each independent wave component, $A_{w,i}$, is derived directly from the energy contained within that frequency bin:

$$A_{w,i} = \sqrt{2S(f_i)\Delta f_i} \tag{2.59}$$

Once the amplitudes are defined, they are combined with an array of randomly generated phase angles $\theta_i \in [0, 2\pi]$. The complete irregular time-series of the free-surface elevation $\eta(t)$ is subsequently reconstructed through the linear superposition of these harmonics:

$$\eta(t) = \sum_{i=1}^{N_\omega} A_{w,i} \cos(2\pi f_i t + \theta_i) \tag{2.60}$$

2.9 Time-Domain Resolution of the Equation of Motion

A WEC and the PTO system can be analysed using a mass-spring-damper model (Fig. 2.3). Given that the buoy is free to move only in the vertical direction, the equation of motion becomes [18]:

$$m\ddot{z} + b\dot{z} + kx = F_{ex}(t) \tag{2.61}$$

The variable m is the sum of the mass of the float and the added mass (A); b comprises the radiation damping coefficient (B) and the PTO damping coefficient (B_{pto}). The position-dependent term comprises, in the case of linear forces, the hydrostatic stiffness term and any spring coefficient K_{pto} of the system. When considering non-linear Froude–Krylov forces, the hydrostatic matrix term K_h is not taken into account, as the excitation forces term includes Froude–Krylov forces in addition to diffraction forces.

$$F_{ex} = F_d + F_{FK} \tag{2.62}$$

To simplify the solution, the added mass and radiative damping were extracted directly at the wave's natural frequency, thereby avoiding the use of the state-space formulation. [19]

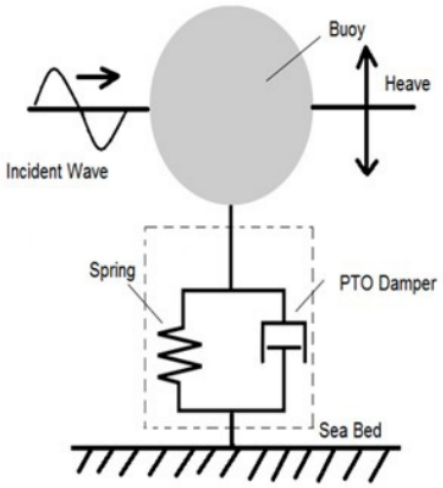


Figure 2.3: Representation of the WEC as a mass-spring-damper system. Source: [2]

To solve Eq. 2.61 , it can be rewritten as a system of two first-order differential equations. Defining the state vector y as the position $y_1 = z$ and the velocity $y_2 = \dot{z}$, follows:

$$\begin{cases} \dot{y}_1 = y_2 \\ \dot{y}_2 = \frac{1}{m}\left(F_{ex}(t) - ky_1 - by_2\right) \end{cases} \tag{2.63}$$

Which can be conveniently rewritten in matrix form $\dot{\mathbf{y}} = \mathbf{A}\mathbf{y} + \mathbf{F}$:

$$\begin{bmatrix} \dot{y}_1 \\ \dot{y}_2 \end{bmatrix} = \begin{bmatrix} 0 & 1 \\ -\frac{k}{m} & -\frac{b}{m} \end{bmatrix} \begin{bmatrix} y_1 \\ y_2 \end{bmatrix} + \begin{bmatrix} 0 \\ \frac{F_{ex}(t)}{m} \end{bmatrix} \tag{2.64}$$

The Eq. 2.64 is integrated into the code at each time step using the second-order Runge-Kutta method,ensuring stable results and low computational cost [20].

Chapter 3

Case Studies and Preliminary Validation under Linear Assumptions

This section defines the geometries under study. In order to ensure their hydrodynamic comparability, these have been selected so as to keep the waterplane area (A_{WP}) and the displaced volume constant. To evaluate the impact of Froude-Krylov forces on the shape and profile of the body, the toolbox has been expanded to include – in addition to the standard cylindrical and conical profiles – spherical profiles of revolution and geometries generated using cubic splines. Specifically, the analyses will focus on three geometries: a cylinder, a sphere and a spline-generated profile. Finally, to verify the reliability of the implemented models, it was necessary to carry out preliminary validations under linear conditions before testing the highly non-linear sea conditions.
These linear verifications were systematically performed for all geometries using both the numerical approach (based on Simpson's 2D quadrature rule) and the closed-form algebraic formulation , evaluating the dynamic coupling in a 3-DoF (surge, heave, and pitch). The main geometric and hydrostatic properties of the analyzed floaters are summarized in Table 3.1

3.1 Validation in Linear Condition

To verify the accuracy of the implementations, it is necessary to compare the NLFK models developed by Simpson and Algebraic with the linear models extracted from the NEMOH software. The linearity conditions considered are imposed differently for the static and dynamic components:

- **Static forces and torques**: Evaluated by imposing infinitesimal body displacements in calm water conditions (no incident waves).
- **Dynamic forces and torques**: Evaluated by keeping the floater fixed at its equilibrium position (zero displacement) while subjecting it to incident waves of infinitesimal amplitude

Table 3.1: Main geometric and hydrostatic properties of the investigated axisymmetric floaters. For the Spline-based buoy, the defining geometrical coordinates represent the control nodes of the cubic Bézier curves.

Property	**Symbol**	**Cylinder**	**Sphere**	**Spline**
Radius at SWL	R_{SWL} [m]	2.625	2.625	2.625
Draft	T [m]	1.964	2.831	3.000
Center of Gravity	z_{CoG} [m]	-1.000	-1.000	-1.000
Reference Point	z_{RefP} [m]	-1.000	-1.000	-1.000
Center of Buoyancy	z_B [m]	-0.982	-1.076	-1.215
Metacentric Height	GM [m]	1.859	1.952	2.091
Waterplane Area	A_{WP} [m^2]	21.647	21.647	21.648
Submerged Volume	V_{Sub} [m^3]	42.524	42.531	42.525
Wetted Surface	S_{Wet} [m^2]	32.400	46.833	42.225

3.1.1 Hydrostatic Stiffness

Under static conditions, when considering a generic axially symmetric solid and imposing an infinitesimal displacement δd, it follows that the static forces FK and moments undergo variations δf.The linear hydrostatic forces acting on the device are mathematically described by the 6×6 hydrostatic stiffness matrix, denoted K_H. This matrix correlates a vector of infinitesimal displacement with 6 degrees of freedom with the corresponding variation in the static Froude-Krylov and gravitational forces. For a generic geometry, the matrix K_H can be fully populated. However, due to the intrinsic geometric properties of the axially symmetric floats considered in this study, the matrix undergoes a drastic simplification.
By aligning the origin of the local reference frame with the vertical axis of symmetry, all off-diagonal coupling terms cancel out analytically. This simplification is demonstrated mathematically by evaluating the surface integrals in cylindrical coordinates. As demonstrated by the calculation of the heave-roll stiffness $K_H(3,4)$ or the roll-pitch stiffness $K_H(4,5)$, these coupling terms require the integration of odd trigonometric functions (e.g. $\sin\vartheta$, $\cos\vartheta$, or their product) over the entire azimuthal domain $[-\pi, \pi]$. These specific integrals cancel out identically.
The only non-zero elements that remain in the 6×6 matrix are the diagonal terms associated with the vertical plane: the heave stiffness $K_H(3,3)$ and the rotational stiffnesses in roll $K_H(4,4)$ and pitch $K_H(5,5)$. Furthermore, due to the device's perfect radial symmetry, the roll and pitch stiffness coefficients are mathematically identical ($K_H(4,4) = K_H(5,5)$).
To calculate the linear coefficient, the NLFK values are calculated before and after applying the infinitesimal displacement, and the final result is compared with the exact solutions derived from [21]:

- $K_h(3,3) = \rho g A_{WP}$
- $K_h(4,4) = K_h(5,5) = \rho g \left(I_{WP} - V_{sub}\overline{\mathrm{BG}}\right)$

where A_{WP} is the water plane area, I_{WP} is the geometric moment of inertia of the water plane area, and $\overline{\mathrm{BG}}$ is the distance between the centres of gravity and buoyancy.

The numerical results of this hydrostatic validation are illustrated in Figure 3.1. As expected from the analytical formulations, the heave stiffness remains identical across all three floaters

due to their equivalent waterplane areas, whereas the pitch stiffness exhibits distinct variations driven by the different vertical positions of their centers of buoyancy.

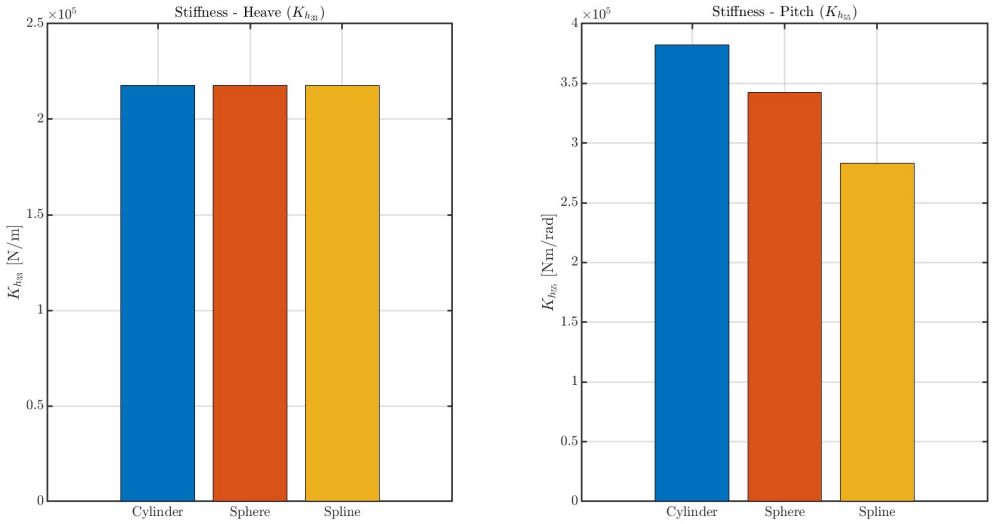


Figure 3.1: Comparison of the hydrostatic stiffness coefficients in heave ($K_{h_{33}}$) and pitch ($K_{h_{55}}$) for the Cylinder, Sphere, and Spline geometries.

3.2 Geometric Defintion

3.2.1 Cylinder

The cylinder is one of the fundamental axially symmetric geometries implemented in the mathematical framework. Its profile of revolution is defined by a constant radius over the entire cross-section of the float, which can be expressed analytically as:

$$f(\varrho) = R \tag{3.1}$$

where R is the constant radius of the cylinder. Consequently, the first derivative of the profile with respect to the local vertical coordinate is strictly equal to zero ($f'(\varrho) = 0$)
The intrinsic advantage of adopting such a simple geometric profile lies in the drastic reduction in the mathematical complexity required to solve the Froude–Krylov integrals. In particular, the zero slope of the lateral surface ensures that the trigonometric term vanishes from the denominator when calculating the upper limit of integration (which represents the instantaneous intersection with the free surface). This mathematical simplification makes the exact algebraic solution in closed form perfectly consistent with the numerical integration, regardless of the magnitude of the pitch angle.
To enclose the solid volume, the floating cylinder is bounded by a flat-bottomed closing disc, the surface parametrisation of which is handled using polar coordinates.

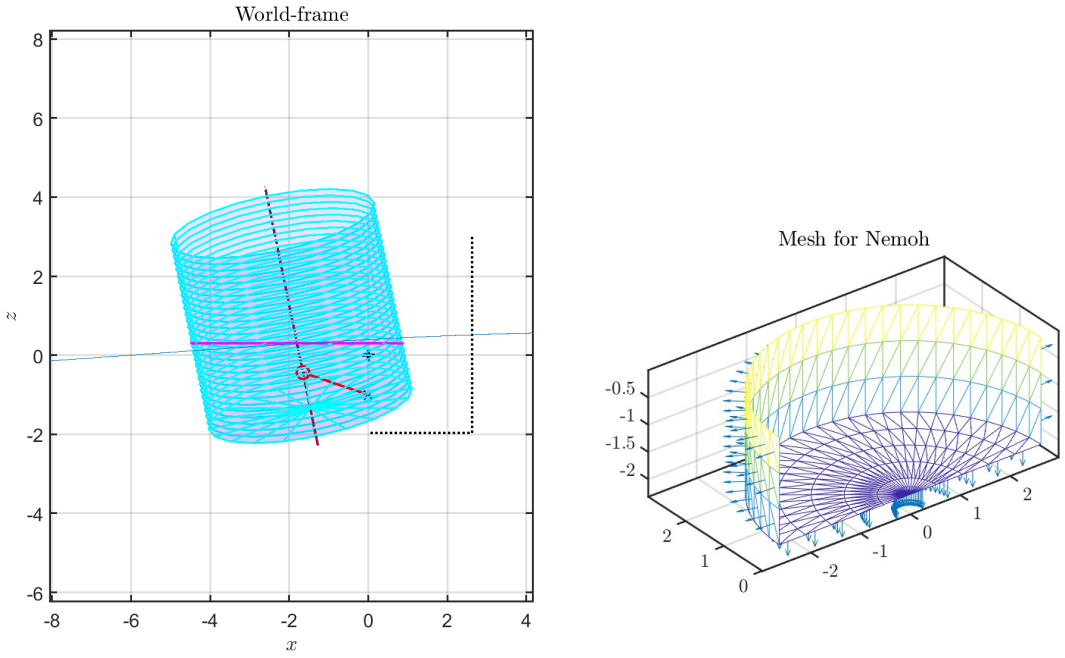


Figure 3.2: Representation of cylindrical geometry under translations and rotations (a). Discretized mesh (b) for the cylindrical floater.

3.2.2 Spherical Geometry

Unlike a cylinder, a sphere has a cross-sectional area that varies with water depth, this variation in volume significantly amplifies the non-linear nature of the Froude–Krylov forces as the displacement of the float changes. Its profile of revolution is described analytically by the equation:

$$f(\rho) = \sqrt{R_s^2 - (\rho - z_{0_sph})^2} \tag{3.2}$$

where R_s is the radius of the sphere and z_{0_sph} represents the distance from the centre of the sphere to the local reference frame (BF). The perfect geometry of the sphere allows benefits to be derived from it if the centre of gravity and the local reference frame are located at the geometric centre of the sphere. Under these conditions, the pressure acting on the surface is directed towards a single point; consequently, this results in the absence of forces that generate moments on the buoy.

The representation of a sphere poses challenges for the numerical solver. The algorithm based on Simpson's quadrature is an adaptive scheme controlled by predefined tolerances. However, in the case of a sphere, the derivative of the geometric profile ($f'(\rho)$) tends to infinity near the poles. This discontinuity creates a mathematical singularity; the polynomial approximation underlying Simpson's method fails to converge in the presence of an infinite gradient. Figure 3.3 shows the spherical floater within the global World-Frame and the corresponding mesh grid utilized by NEMOH

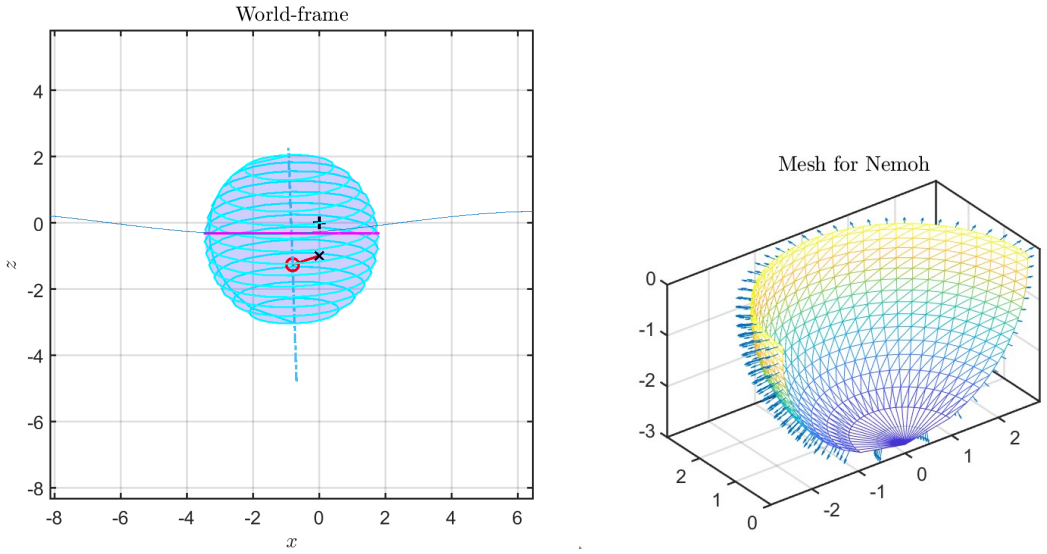


Figure 3.3: Representation of spherical geometry (a). Discretized mesh (b) for the spherical floater.

3.2.3 The Spline-Based Buoy

In the design and optimisation of WECs, the integrated approach that combines the optimisation of the float's geometry with that of the control system is proving to be fundamental to maximising energy extraction. As highlighted by [22], in order to optimise the shape of the buoy in a realistic manner, it is essential to evaluate non-linear hydrodynamics, utilising in particular static and dynamic Froude-Krylov forces. However, the continuous calculation of non-linear forces on geometries that change iteratively during an optimisation process can lead to a large computational cost. Applying non-linear Froude-Krylov forces to new geometries allows us to explore new shapes and rapidly assess their effects on performance. In order to explore and optimise new geometries whilst ensuring computational efficiency, an axially symmetric profile defined by cubic splines has been implemented. The use of splines allows the shape of the float to be parameterised in a continuous, smooth and versatile manner.
The revolution profile of the cubic spline in the NLFK4ALL framework is obtained using Bézier curves. It is defined parametrically by a set of four control points (P_0, P_1, P_2, P_3) which weight the basic Bernstein polynomials as a function of a dimensionless variable $t \in [0, 1]$ [23].
NLFKALL does not accept parametric rotational profiles; instead, a cubic profile must be generated as follows:

$$f(\rho) = a\rho^3 + b\rho^2 + c\rho + d \tag{3.3}$$

Within the toolbox, the definition of the geometry is based on the compilation of a coordinate matrix, denoted as xz [10].
In the specific case of parameterisation using cubic splines, it is important to note that the values entered in this matrix do not represent pairs of coordinates that physically belong to the geometry's profile, but rather define the control points of the Bézier curve. These are followed by further pairs of coordinates, which are required to define the closures of the floater.
It is therefore necessary to convert the parametric coordinates of the Bézier curves into an explicit one-dimensional expression for the radius as a function of depth $(X = f(\rho))$.
The trend of the vertical coordinate of the spline depends on the parameter $t \in [0, 1]$ according

to the Bernstein polynomial basis:

$$Z(t) = (1-t)^3 P_{z0} + 3t(1-t)^2 P_{z1} + 3t^2(1-t) P_{z2} + t^3 P_{z3} \tag{3.4}$$

To linearise the dependence of Z on the Bézier curve parameter t, the control points along the z-axis are positioned at equal distances from the final reference elevation. Equation 3.4 then becomes:

$$Z(t) = t \cdot Z_d = \rho + z_{RefP} \tag{3.5}$$

Once this direct proportionality between the spatial coordinate ρ and the parameter t has been established, the radial equation $X(t)$ is decoupled by means of discretisation and numerical fitting. The parametric domain is evaluated using a high-resolution vector, extracting pairs of coordinates (ρ_i, X_i) that accurately describe the profile, on which a third-degree polynomial regression using the least squares method is then performed. In this way, the coefficients (a, b, c, d) are obtained, which allow the radius of the body to be expressed via the continuous polynomial $X = f(\rho)$ (Eq. 3.3). By using the rotational profile shown in the Fig. 3.4, it is possible to

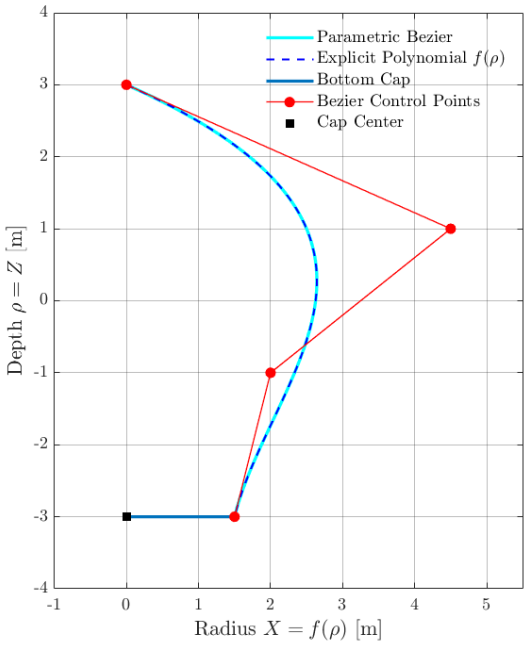


Figure 3.4: Graphical representation of the revolution profile using nodes of Bèzier for a cubic spline as a function of $f(\rho)$

obtain a representation of the geometry known as 'SplineBuoy', whilst maintaining the same water-displacement area at the surface and the same volume of displaced water. A major advantage of this Bézier-based implementation is its considerable flexibility within the code. By simply modifying the coordinates of the control points in the xz matrix, it is possible to quickly generate and simulate new spline-based geometries with different slopes and profiles. The buoy studied in this work is shown in the figure:

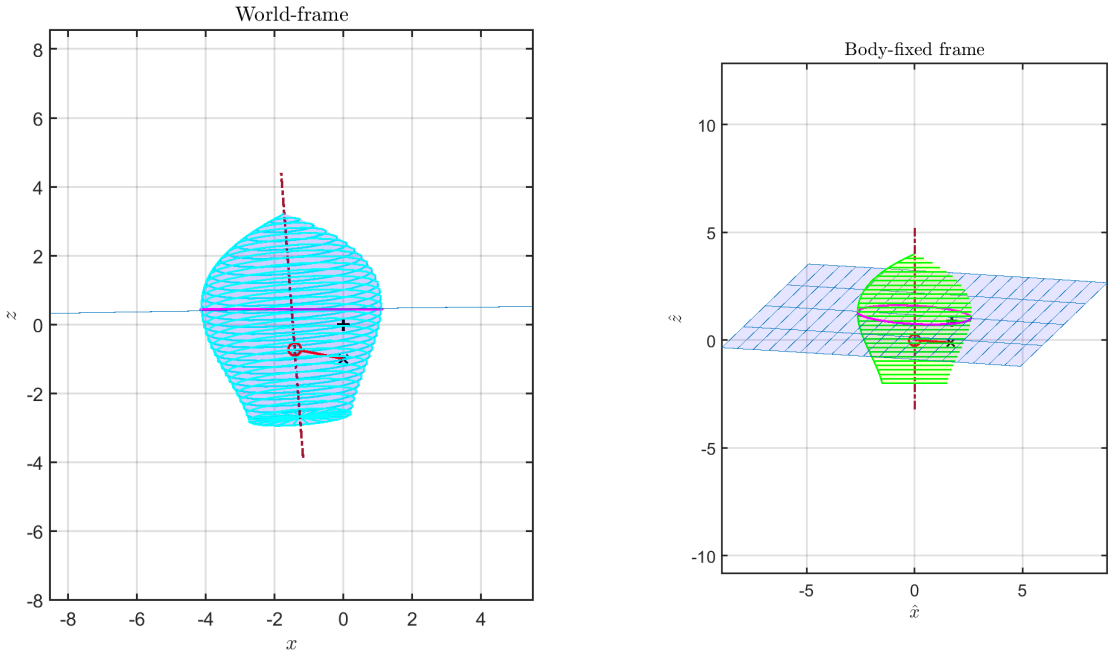
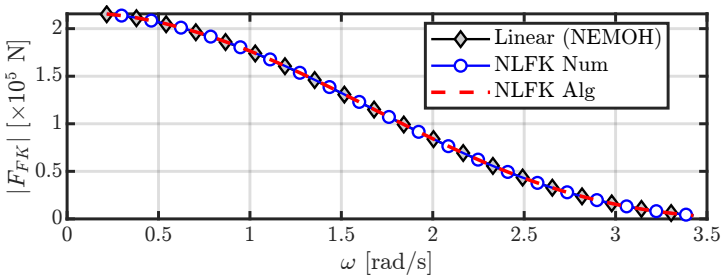


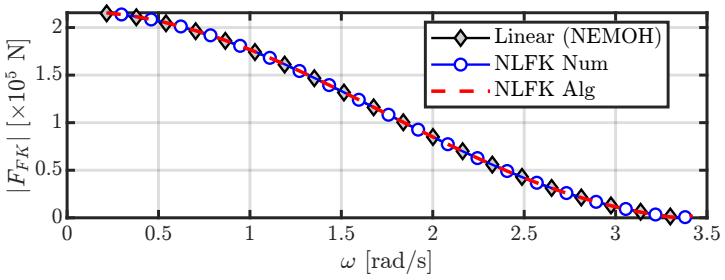
Figure 3.5: Representation of 'SplineBuoy' geometry under translations and rotations in the Word Frame (left) and Body Frame (right).

3.3 Dynamic Linear Validation

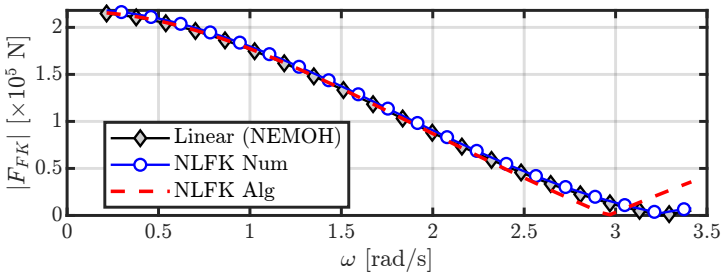
The robustness of the models presented is ensured by verifying the dynamic forces of FK under linear conditions, by imposing zero displacement and an incident wave with a small amplitude. The figure 3.6 compares the amplitudes of the Froude–Krylov dynamic excitation force in the heave direction across the frequency domain for the three geometries investigated: Cylinder (a), Sphere (b) and Spline (c). In general terms, it can be observed that the three floats exhibit an extremely similar frequency response: the force is maximum at low frequencies (approximately 2.1×10^5 N) and decays asymptotically to zero for frequencies greater than $\omega = 3.5$ rad/s. This strong physical similarity is entirely consistent with the criteria imposed during the geometric design phase. Since the three floats were parameterised to have the same displaced volume and the same buoyant area at rest, the overall vertical wave force is effectively equivalent in the linear regime. Furthermore, it is crucial to note that, for all three geometries, the NLFK numerical method overlaps perfectly with the results provided by the reference linear BEM solver across the entire frequency spectrum. This result definitively validates the robustness and accuracy of the 2D Simpson integration algorithm implemented in the toolbox. Although the numerical model proves to be stable, the application of the algebraic method reveals clear differences linked to the geometric profile of the body and to the mathematical limitations of its very formulation. As regards simple geometries such as the cylinder or the sphere, the algebraic solutions are able to approximate the behaviour of the float at frequencies of $3.5 rad/s$. The spline is generated using a profile of revolution characterised by a third-degree polynomial; however, the solutions to the FK integrals calculated using infinite Bessel expansions are truncated to the first few orders to avoid polynomials of too high a degree. The truncation of these functions leads to instability at frequencies greater than $2 rad/s$ for the spline geometry, whilst the numerical method remains stable but requires a higher computational cost.



(a) Cylindrical Floater



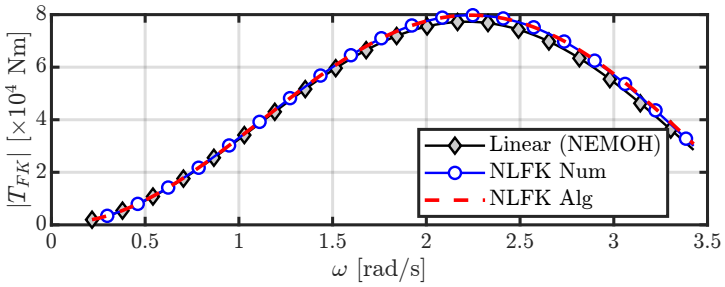
(b) Spherical Floater



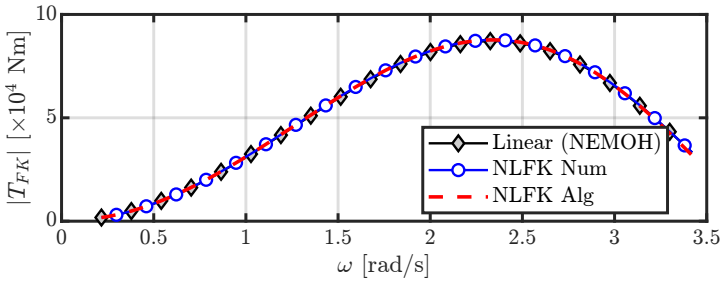
(c) Spline-based Floater

Figure 3.6: Comparison of dynamic Froude-Krylov Heave excitation forces at different frequency for the three analyzed geometries.

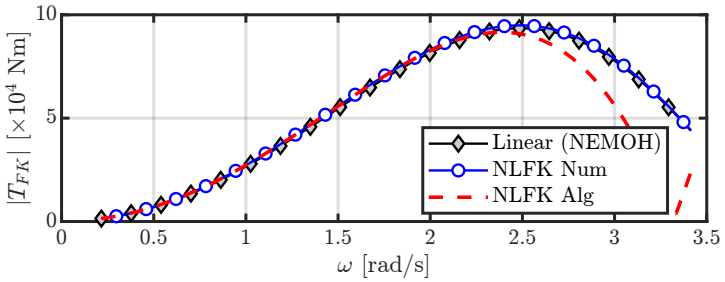
This instability is most clearly evident in the Fig. 3.7c showing the pitch torque.



(a) Cylindrical Floater



(b) Spherical Floater



(c) Spline-based Floater

Figure 3.7: Frequency-domain comparison of dynamic Froude-Krylov pitch torques for the three analyzed geometries

The pitch excitation torque (Fig. 3.7) is mathematically determined by the cross-product of the position vector and the normal to the surface (2.53) . Consequently, it is highly sensitive to the spatial distribution of the surfaces and their depth relative to the centre of rotation ($z_{Ref} = -1$ m). The cylinder exhibits the lowest peak moment (approximately 8×10^4 Nm), whilst the sphere reaches 9×10^4 Nm and the spline records the highest excitation torque, approaching 10×10^4 Nm.
This result highlights the complex interaction between the dynamic pressure field and the geometric lever arms of the float. The dynamic pressure decays exponentially with depth (e^{kz}). The flat bottom of the cylinder, situated at a shallow draught of 1.96 m, is subjected to higher dynamic pressure. However, its distance from the centre of rotation is relatively small (less than 1 m). In contrast, the spline geometry has a significantly greater draught (3.00 m). Although the wave pressure at this depth is exponentially weaker, the tip of the spline is situated 2 me-

tres away from the reference centre. This vertical lever arm, combined with the extended and inclined lateral surfaces, amplifies the resulting torque, enabling the spline to capture a greater overall exciting moment than the other geometries.
The Fig. 3.7a shows that the linear torque differs slightly from that calculated using the NLFK models; this is because a slightly larger number of panels must be considered for the cylinder in order to accurately represent the response under dynamic conditions. (350 panels are sufficient) As regards the sphere, torques occur when, due to the selected geometry and conditions, the reference centre does not coincide with the geometric centre.
Figure 3.8 illustrates a comparison of the amplitude and phase of the Froude-Krylov excitation

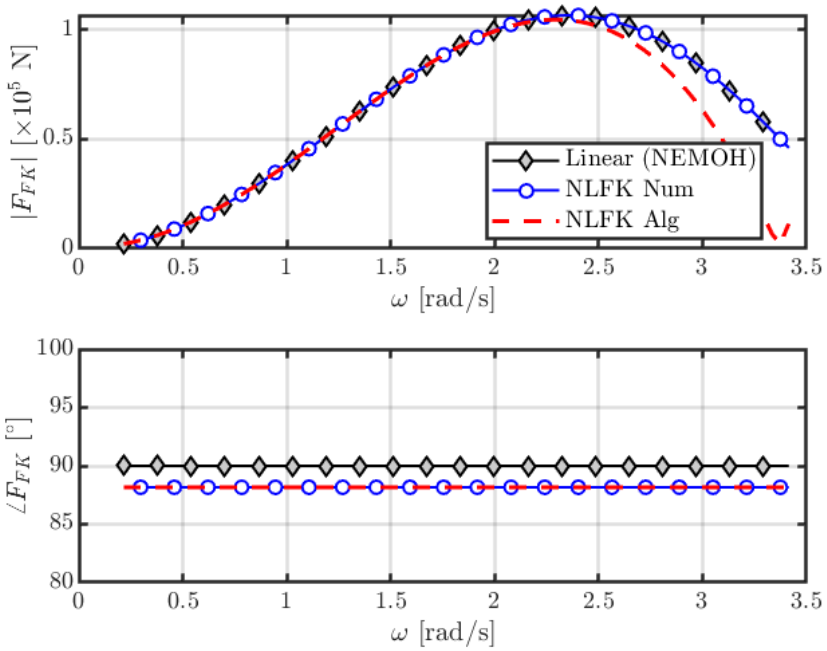


Figure 3.8: Comparison of the dynamic Froude-Krylov surge excitation force ($|F_{FK}|$) and its phase for the Spline-based floater.

force in Surge for the float with a spline profile. Analysing the trend in the amplitudes (upper graph), the behaviour is entirely analogous to that previously discussed for the pitch moment. The numerical solver based on Simpson's quadrature follows the reference curve of the linear BEM model (NEMOH) with absolute precision across the entire frequency spectrum. The algebraic method, by contrast, matches the reference curve excellently in the medium-to-long-wave regime, before diverging sharply at high frequencies ($\omega > 2.5$ rad/s). This deviation is the natural consequence of truncating the Bessel series; indeed, both the surge force and the pitch moment depend on the integration of the same first-order asymmetric harmonic (J_1). As regards the phase analysis, the curves maintain a flat and consistent trend. A very slight, constant deviation is visible between the theoretical linear solution (exactly at 90°) and the results obtained from the NLFK models. This minimal shift is linked to the temporal sampling resolution used during the validation simulations.

3.4 Check in Irregular Waves

When evaluating Froude-Krylov forces under irregular wave conditions, the direct coupling of highly non-linear hydrodynamic forces with time-domain motion integration can sometimes lead to numerical instabilities or non-physical kinematic results.
To overcome this problem and robustly isolate the force calculation, the linear RAO method is used to precalculate the entire time history of the WEC's kinematic displacements based on the spectrum of the incident waves. Once this linear motion has been generated, it is saturated using predefined operational constraints so that the kinematic vector remains within a physically consistent and safe domain.
The calculation of the RAO requires a mass vector distribution as (Sect. 2.4); consequently, the mass of the float has been assumed to be equal to the mass of the displaced volume of water, whereas the pitch inertia has been set at 10 times the mass in order to obtain physically consistent results and to prevent immediate saturation at the specified constraints. In the following section, the various geometries implemented using both the algebraic and numerical NLFK models by Simpson are compared with the linear response from Nemoh.
Given pre-calculated kinematic states, the NLFK4ALL framework computes the exact instantaneous nonlinear Froude-Krylov forces across a standardized simulation window of 1,000 time steps.
In the simulations, the peak period (T_p) was calculated as the arithmetic mean of the resonance frequencies for heave and pitch, derived from the respective peaks of the RAO operators. Furthermore, the significant wave height (H_{m0}) was constrained to 65% of the buoy's nominal draught. This constraint ensures that the device behaves predominantly as a *wave-follower*, following the wave profile without the bottom becoming exposed or the buoy becoming fully submerged. By keeping the wetted geometry roughly constant, drastic changes in the submerged volume are avoided and, consequently, extreme non-linear effects are kept to a minimum. In this operating context, Figure 3.9 illustrates the kinematics (upper panels) and the Froude–Krylov excitation forces (lower panels) for the spherical float, simulated in the complete 3-degree-of-freedom configuration (Surge, Heave and Pitch).

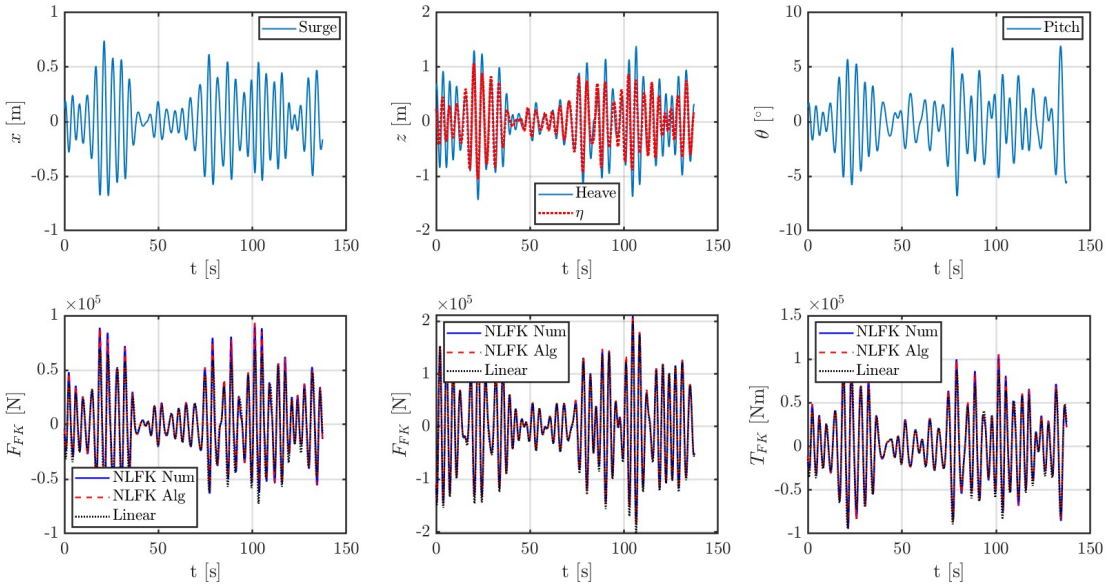
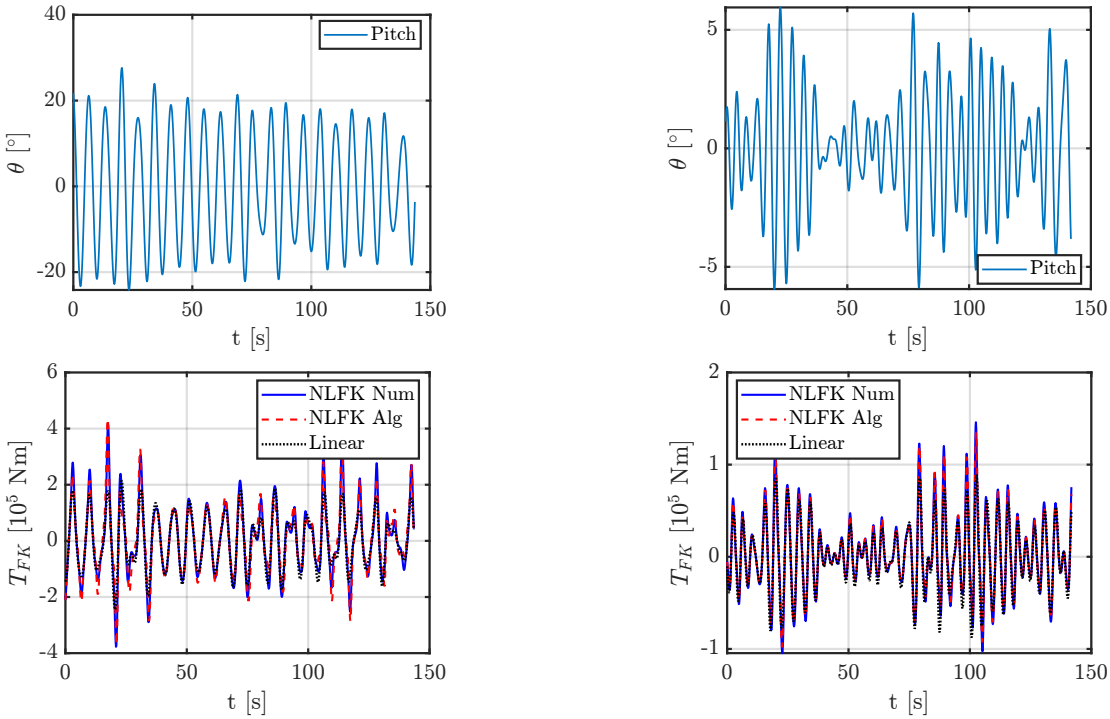


Figure 3.9: Time-domain kinematics (top panels) and Froude-Krylov excitation forces (bottom panels) for the spherical floater in a 3-DoF configuration (Surge, Heave, and Pitch)

The Fig. 3.10 shows specific results for the rotations and pitch torques between the cylinder and the float with a profile generated by a spline. The greater draft and the tapered shape of the Spline geometry result in a significantly higher radiation damping coefficient (B_{55}) than the cylinder. This dissipative effect governs the different pitch dynamics observed: as defined by the respective RAO operators, the kinematic response of the cylinder is subject to large excursions, whereas the Spline configuration ensures considerable rotational stability.
As observed in time-domain simulations, the magnitude of pitch rotation plays a crucial role in the divergence between linear and non-linear hydrodynamic models. In the case of small displacements, linear potential theory calculates the Froude–Krylov excitation moments on an average, constant wetted surface. However, when the float undergoes large rotational excursions, such as those observed for the cylindrical geometry, the instantaneous wetted area undergoes significant geometric alterations. During a large pitch movement, one side of the buoy submerges deeper into the fluid, exposing a larger area to the exponential dynamic pressure field, whilst the opposite side emerges. Consequently, both the position vectors and the vectors normal to the surface used to calculate the moment undergo significant spatial variations. By integrating the pressure field over the exact instantaneous wetted surface, the NLFK approach captures these asymmetric load distributions and the continuous variation in the geometric lever arms. This physically accurate representation leads to significant deviations in the magnitude of the calculated NLFK excitation torque compared with simplified linear estimates, which inherently fail to account for the changing geometry.



(a) Cylinder **(b)** Spline

Figure 3.10: Comparison of pitch kinematics (top) and excitation moments (bottom) between the Cylinder and the Spline geometries under irregular wave conditions.

The geometries under consideration are defined by their respective curves of revolution, ranging from simple forms with vertical walls (Cylinder) to highly non-linear profiles (Sphere and Spline). The use of such curved profiles increases the polynomial order of the integrands defining the Froude-Krylov expressions, increasing the computational complexity. In this scenario, the numerical solver based on Simpson's adaptive quadrature encounters increasing computational difficulties. For non-cylindrical geometries, in fact, the numerical algorithm is forced to continually iterate and refine the spatial discretisation of the integration domain in order to meet the tolerances imposed. The execution times for calculating the hydrodynamic forces for the three geometries tested are summarised in the following table:

Table 3.2: Comparison of computation times for simulations of irregular waves over 1,000 iterations.

Geometries	**NLFK Num [s]**	**NLFK Alg [s]**
Cylinder	3.75	0.24
Sphere	6.46	1.48
Spline	47.55	11.33

Chapter 4

Time-Domain Simulations and Performance Analysis

The model validation carried out in the previous sections have enabled a more stable and robust implementation of the non-linear Froude-Krylov force calculation within time-domain simulations. In this section, the dynamic responses of the various geometries are compared under regular wave conditions. The decision to consider a regular wave allows for a clear, basic verification of the code and provides a direct benchmark for assessing the computational efficiency of the proposed numerical and algebraic methods, whilst avoiding the superimposed complexities of irregular sea states.
The various floating bodies — whose properties were defined in Section 3.1 — are evaluated by coupling them to a Power Take-Off (PTO) damping system, in order to assess their energy extraction capabilities. The time resolution of the equations of motion, from which the results presented here are derived, was carried out using a second-order Runge-Kutta numerical integration scheme.
The simulations presented in this section relate to the dynamic response of a two-degree-of-freedom model, restricted to the motions of heave and pitch.

4.1 Simulation Setup

In order to rigorously assess the impact of non-linear hydrodynamic forces on the performance of the converters, time-domain simulations were carried out by subjecting the various geometries to a series of regular waves. All simulations were set up assuming a constant depth of $h = 300$ m. This depth ensures the applicability of the deep-water assumption ($h > \lambda/2$) across the entire frequency range analysed, allowing the wavelength λ and the kinematics of the water particles to be calculated independently of the influence of the seabed.
In order to isolate the non-linear effects associated with the device, the wave steepness (H/λ) was set to 0.018, a parameter that realistically describes the normal operating conditions of WECs [24].
As regards pitch inertia, a value consistent with the geometry of the simulated floats is assumed, considering an inertia equal to three times the mass of the device. Increasing the inertia reduces the pitch resonance frequency, thereby creating greater resistance to rotational motion.
During time-step simulations, models based on the calculation of FK forces compute an instantaneous buoyant surface. Following large pitch excursions, the hydrostatic buoyancy moments are reduced, inducing large rotations in the buoy. To prevent it from capsizing, it is necessary

Table 4.1: Wave periods and corresponding wave heights used in the simulations.Steepness($s = 0.018$).

Wave Period T_w **[s]**	**Wave Height** H_w **[m]**
3.0	0.25
4.0	0.45
5.0	0.70
6.0	1.01
7.0	1.38
8.0	1.80
9.0	2.28
10.0	2.81

to simulate the reactions of a mooring line during pitch rotations. Therefore, a supplementary restoring stiffness of $K_{moor} = 3 \times 10^4 Nm/rad$ is assigned to the pitch motion to account for the structural mooring limits.

Table 4.2: Properties and mooring of the three geometries.

Mass (M) **[kg]**	**Inertia** (I_5) **[kg m^2]**	**Mooring Heave** ($K_{moor,33}$) **[N/m]**	**Mooring Pitch** ($K_{moor,55}$) **[Nm/rad]**
4.36×10^4	1.31×10^5	1.00×10^4	3.00×10^4

4.2 Free decay test

For each geometry, free decay tests are carried out in heave, setting an initial displacement of 3 metres, and in pitch, setting an initial rotation of 10 degrees. These tests allow us to see, in the absence of waves, how the system responds and interacts according to its dynamic characteristics.
The aim of the analysis is to evaluate the transient behaviour of the system and to determine its natural frequencies – quantities closely linked to mass (in the case of translational motion) and moment of inertia (in the case of angular motion). A key parameter in governing the magnitude and duration of these oscillations is radiative damping. This hydrodynamic component, which varies significantly depending on the specific geometry of the device, typically takes on negligible values at low frequencies. From a physical point of view, this indicates that the float, whilst moving slowly, radiates a wave field of small magnitude, effectively limiting the dispersion of energy into the surrounding environment (Fig.4.1). The values shown in Table 4.3 indicate

Table 4.3: Comparison of the natural periods in Heave and Pitch for the three geometries.

Geometry	**Heave** T_n **[s]**	**Pitch** T_n **[s]**
Cylinder	3.68	3.98
Sphere	3.43	3.98
SplineBuoy	3.38	4.38

that the natural periods of the floats are consistent with their geometry and spatial distribution.

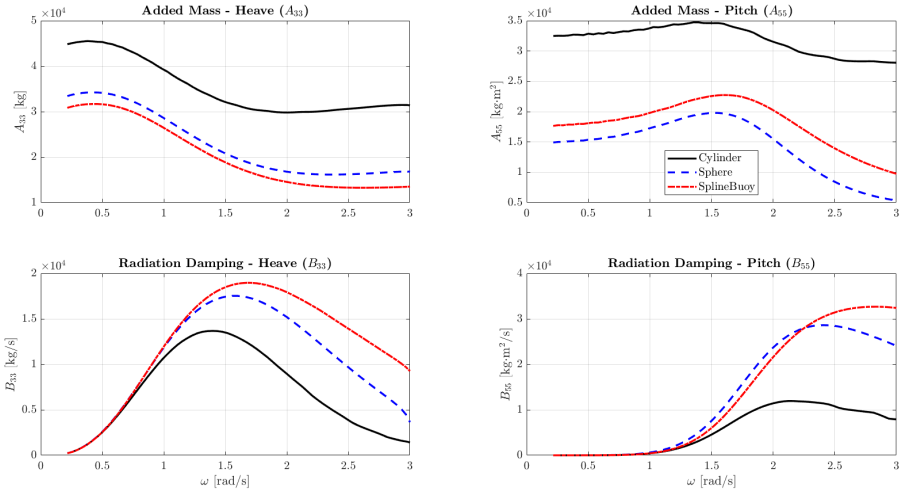
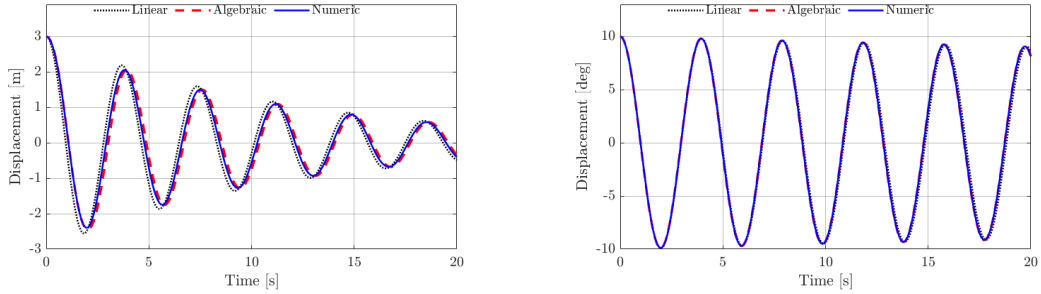


Figure 4.1: Frequency-dependent hydrodynamic coefficients evaluated via the BEM solver (NEMOH) for the Cylinder, Sphere, and SplineBuoy geometries. The top panels illustrate the added mass in heave (A_{33}) and pitch (A_{55}), while the bottom panels show the corresponding radiation damping coefficients (B_{33}, B_{55}).

As regards the heave motion, the results show a perfect linear correlation between the coefficients and the system's responses. Since the natural period T_n is directly influenced by the total mass of the body, it is expected that higher values of added mass will correspond to slower oscillations. Looking at Fig. 4.1, the Cylinder has the highest added mass values A_{33}, followed by the Sphere and, finally, the Spline. This is consistent with the values shown in Table 4.3: the Cylinder has the longest natural period (3.68 s), whilst the SplineBuoy is the fastest (3.38 s). In this degree of freedom, the added mass clearly determines the difference in periods.
With regard to pitch motion, it is necessary to pay attention to another fundamental parameter. In this case, the natural period does not depend solely on the total inertia (given by the sum of the physical inertia and the added inertia A_{55}), but is inversely proportional to the hydrostatic restoring stiffness of the float. Although the graphs show that the Cylinder has significantly greater added inertia in pitch than the other two shapes, the table reveals that the SplineBuoy has the longest natural period of all (4.38 s). This behaviour indicates that, in pitch motion, it is the hydrostatic stiffness that dominates the dynamics. The SplineBuoy, despite having an intermediate level of added inertia, possesses a considerably lower hydrostatic restoring moment, which makes it slower to return to its original position and prolongs its period of oscillation.

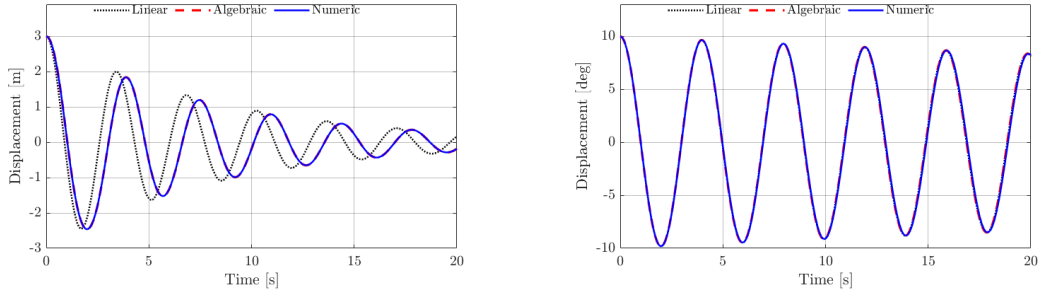
Cylinder



(a) Heave displacement **(b)** Pitch displacement

Figure 4.2: Free decay test for the cylinder over time, comparing Linear, Algebraic, and Numeric models.

Sphere

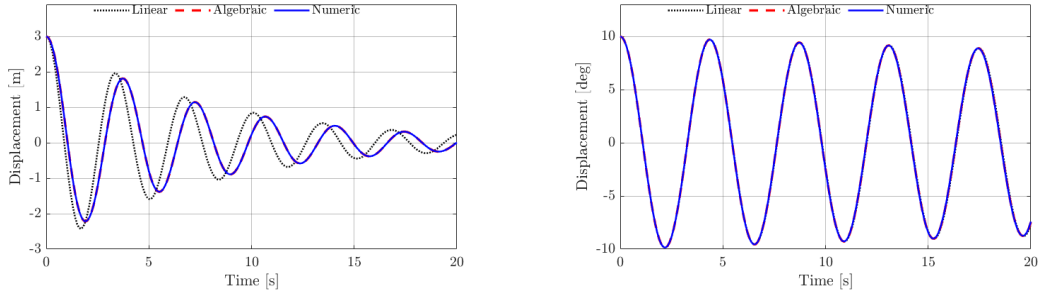


(a) Heave displacement **(b)** Pitch displacement

Figure 4.3: Free decay test for the sphere over time, comparing Linear, Algebraic, and Numeric models.

Spline

In Figure 4.2a, it can be seen that for the cylinder, the NLFK models overlap with the linear model; this is because the cylinder has a cross-section that remains constant along its depth, and consequently its hydrostatic stiffness also remains unchanged. For the spline and the sphere (Fig. 4.4a and Fig.4.3a), the linear model predicts a shorter oscillation than the numerical and algebraic models. This occurs because the sphere and the spline have a highly variable buoyant cross-sectional area. Moving the body by 3 metres causes the buoyant area to change drastically, significantly altering the hydrostatic restoring stiffness. It is also important to note that, under these conditions, the algebraic and numerical models match perfectly; despite the simplifications in the algebraic NLFK model, it manages to describe exactly what is happening more quickly than the numerical model.
In terms of pitch, however, all three models match perfectly. This is due to the low oscillation, which does not differ significantly from the linear model. The high mooring stiffness dominates the slight hydrostatic non-linearities, forcing the system to behave linearly.
With regard to heave, it can be seen that the decay in amplitude is extremely slow for all three figures; this is due to the low radiation damping values for all three geometries.



(a) Heave displacement

(b) Pitch displacement

Figure 4.4: Free decay test for the spline over time, comparing Linear, Algebraic, and Numeric models.

4.3 PTO Control Strategies

The conversion of the mechanical energy of wave motion into useful power takes place, within WECs, through the installation of mechanisms known as Power Take-Off. The performance of these systems depends heavily on the control strategies employed, which modulate the force of the PTO to amplify the motion of the float and drive it into resonance with the incident wave, thereby maximising the energy extracted.
To examine the non-linearities of the Froude–Krylov forces, in the following sections the three geometries are subjected to different conditions:

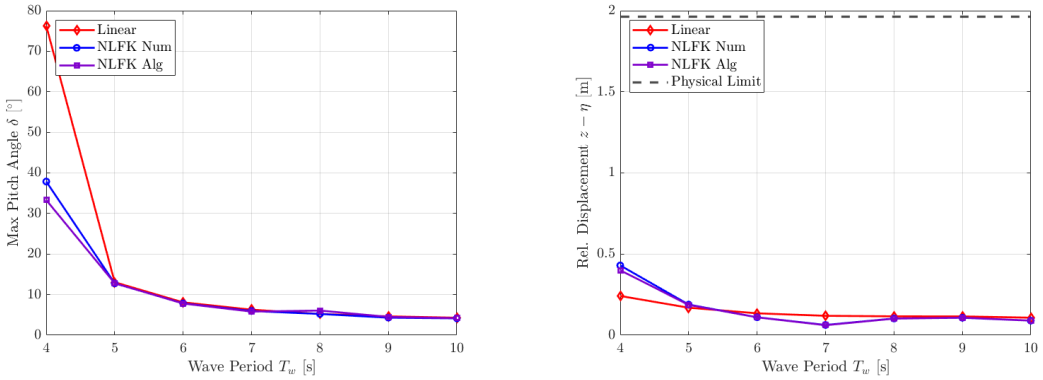
- Without Control
- Passive Control
- Reactive Control

As highlighted by [16], non-linearities are greater when an aggressive control strategy is used, such as reactive or latching control. However, depending on the shape of the float and its ability to rotate about the pitch axis, non-linear phenomena arise. The aim of this study is to examine how non-linearities vary with the control and with the geometry, by comparing the non-linear models with the linear solutions.

4.3.1 Uncontrolled Response

Although, in the absence of a control system, the kinematic excursions of the float are not maximised, this basic configuration already allows us to observe clear resonance phenomena and to highlight the marked differences in predictions between linear theory and non-linear models.

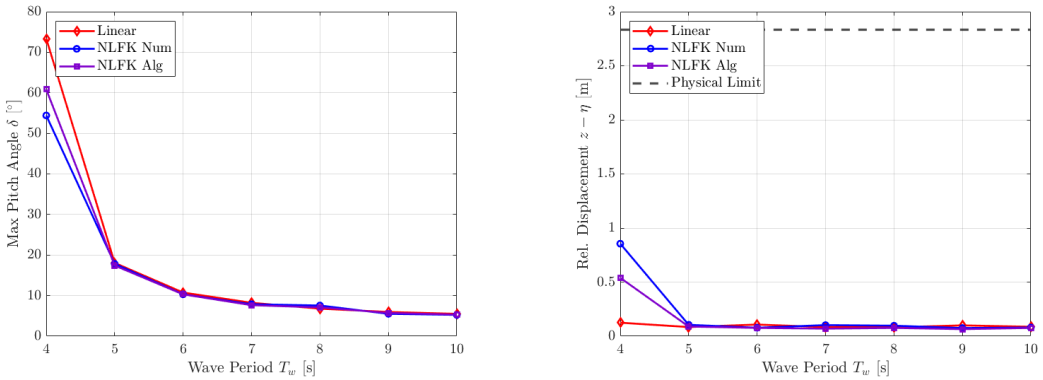
Cylinder



(a) Maximum Pitch Angle **(b)** Relative Heave Displacement

Figure 4.5: Uncontrolled dynamic response of the cylinder across different wave periods.

Sphere

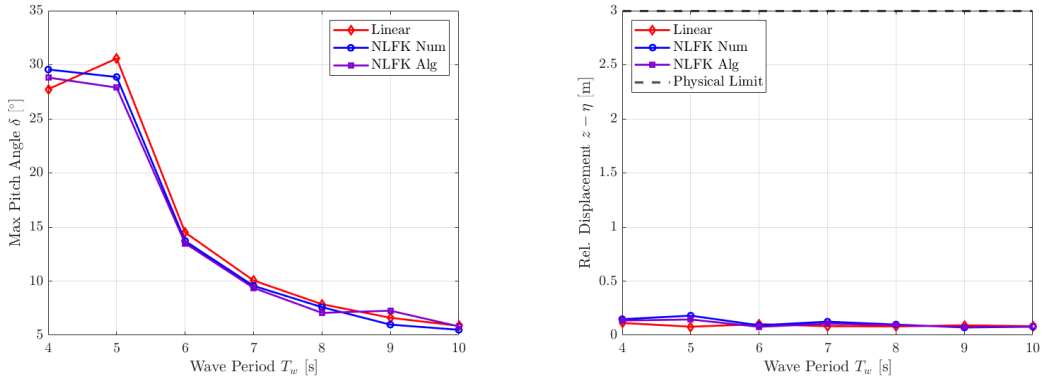


(a) Maximum Pitch Angle **(b)** Relative Heave Displacement

Figure 4.6: Uncontrolled dynamic response of the sphere across different wave periods.

Spline

For all three buoys, it is evident that, in the absence of controls, the very low relative displacement indicates that the buoy follows the wave. The wetted area does not vary along the buoy's draught. The only significant exception is observed for the sphere (Fig. 4.6b), where at $T_W = 4s$ the numerical model records a displacement of almost 1 m. At this wave period, the system coincides almost perfectly with its natural pitch period, generating large rotations.
As the buoy's centre of gravity lies 1 metre below the water level and not at its geometric centre, the buoy undergoes oscillations. This rotation displaces the wetted volume; consequently, the sphere no longer behaves as a wave follower, generating a greater relative displacement compared to other wave periods. The algebraic model attempts to represent this phenomenon, but the assumption of small rotations in pitch leads to an underestimation of this behaviour.
In the Figure 4.6a, it can be seen that the linear model overestimates the rotations. This occurs



(a) Maximum Pitch Angle

(b) Relative Heave Displacement

Figure 4.7: Uncontrolled dynamic response of the spline across different wave periods.

because the linear theory evaluates the forces by assuming that the sphere always remains in its initial equilibrium position. In the NLFK model, however, the moments acting on the buoy are calculated instant by instant over the exact wetted surface. This continuous redistribution of the pressure field alters the magnitude and arms of the moments, mitigating the effect of resonance and yielding physically more moderate rotations.

The cylinder (Fig.4.5), being subjected to forces at its natural pitch period, exhibits large rotations which linear theory tends to significantly overestimate. By contrast, NLFK models limit the angle amplitude to more realistic values, as the instantaneous update of the pressure field accurately captures the variation in lever arms and the resulting dynamic coupling with the heave motion. From a mathematical point of view, it should be noted that, although the algebraic solver's general formulation relies on the small-angle approximation to analytically resolve the upper integration limit with the free surface, the specific constant-radius geometry of the cylinder removes the trigonometric terms from the denominator. While this geometric peculiarity makes the algebraic formulation remarkably accurate across most of the frequency spectrum, a slight discrepancy with the numerical model emerges at extreme resonant rotations (e.g., at $T_w = 4$ s).

The slight discrepancy observed in the resonance analysis is attributable to the analytical integration of the Froude–Krylov dynamic pressure field. To obtain a closed-form solution, the algebraic formulation of the dynamic pressure is based on the assumption of small pitch angles; whilst this assumption can be resolved for the static forces thanks to the cylinder's profile of revolution, it cannot be resolved for the dynamic forces. In the absence of control strategies, Figure 4.7 shows that, unlike the other geometries, the spline is not subject to extreme rotations. The natural pitch period of the buoy falls between 4 and 5 seconds; however, its specific shape and greater draught provide higher radiation damping compared to the other geometries. Under these conditions, the spline behaves as an excellent wave-follower in heave. Furthermore, because the pitch amplitude remains constrained, nonlinear geometric effects are minimal, allowing the predictions of the linear model to perfectly coincide with both NLFK models.

The considerations outlined so far regarding relative displacements and rotations reflect the behaviour of the RAO in heave. As illustrated in Fig. 4.8, in the absence of control, the devices tend to behave as wave-followers. Since the kinematic excursions are limited under these conditions, the non-linear effects are not emphasised. Therefore, there is a need to implement control strategies to better highlight these effects.

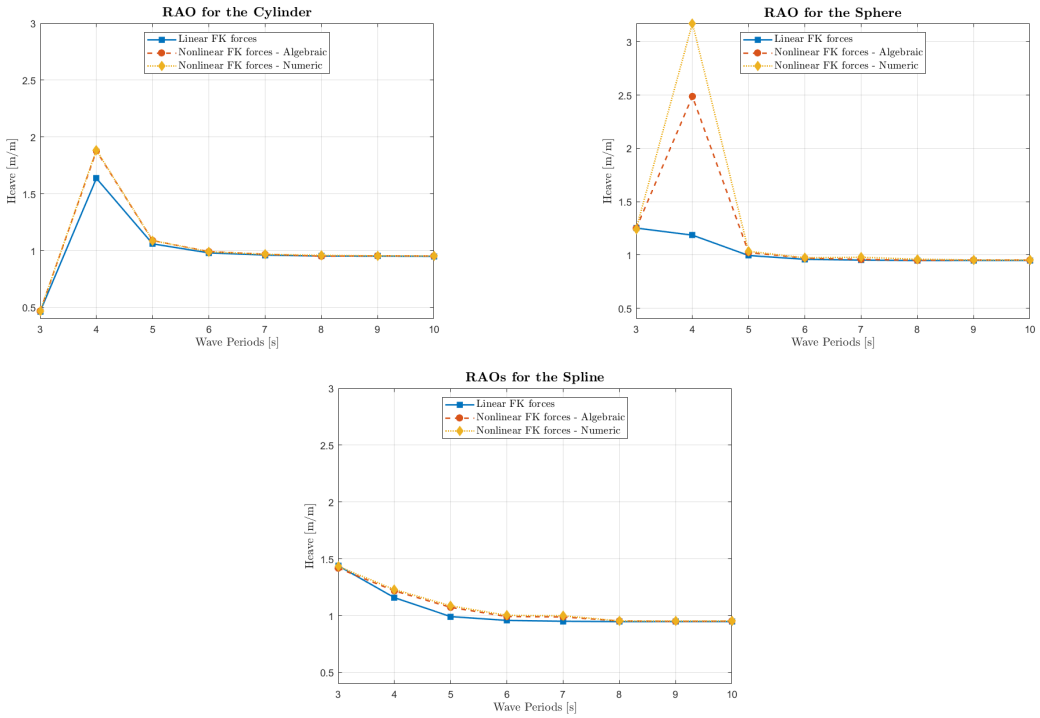


Figure 4.8: Comparison of RAOs (Response Amplitude Operators) for the various geometries analysed.

4.3.2 Passive Control

In this section, the PTO is modelled as a linear damper. Therefore, F_{PTO} is controlled only by the PTO's damping coefficient (B_{PTO}), which is proportional to the heave velocity [25].
The optimal damping coefficient of the PTO (B_{PTO}) is determined through a parametric analysis on a discrete set of values, identifying, for each geometry, the value that maximises the extracted power. In order to minimise the computational cost, and given the marginal discrepancies found compared with the NLFK models (both numerical and algebraic), the search for optimal solutions is carried out using linear simulation alone.
The simulations for the three geometries are carried out for different wave periods, with a fixed steepness of $s = 0.018$.
The control strategy adopted, which is purely resistive in nature, is not particularly aggressive and does not induce excessive kinematic excursions relative to the wave motion. Nevertheless, analysis of the pitch degree of freedom reveals marked non-linear effects. Specifically, the absence of a viscous damping term in the mathematical model leads to large rotations of the float, resulting in unrealistic estimated responses under certain wave conditions. This sensitivity to pitch instability has been studied in the literature by taking viscous forces into account.[16]

Cylinder

The figure 4.10 shows the kinematic response for heave displacement and for maximum pitch rotations at different wave periods for the cylinder. The graph shows that purely passive control limits the vertical excursions. Consequently, the models overlap each other. The constant geometry across the entire drafts confirms that, for a cylindrical buoy, the effect of non-linear

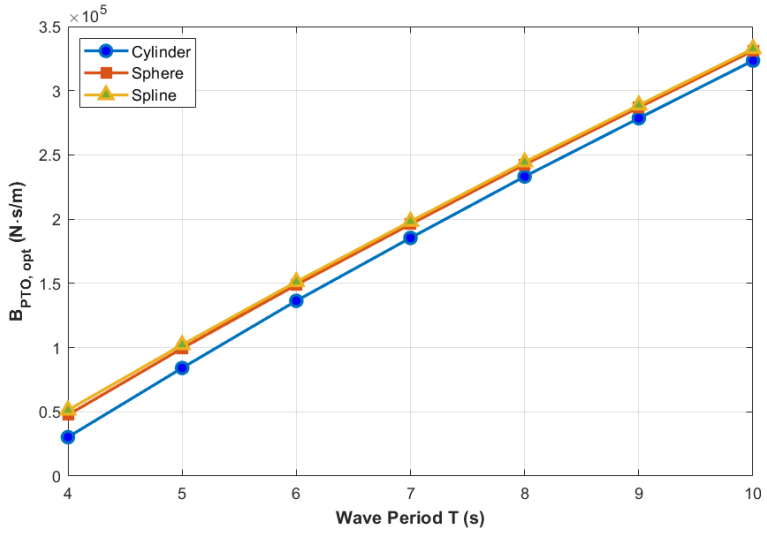


Figure 4.9: Trend in the optimal PTO damping coefficient ($B_{PTO,opt}$) as the wave period T varies for the three different geometries (Cylinder, Sphere, Spline).

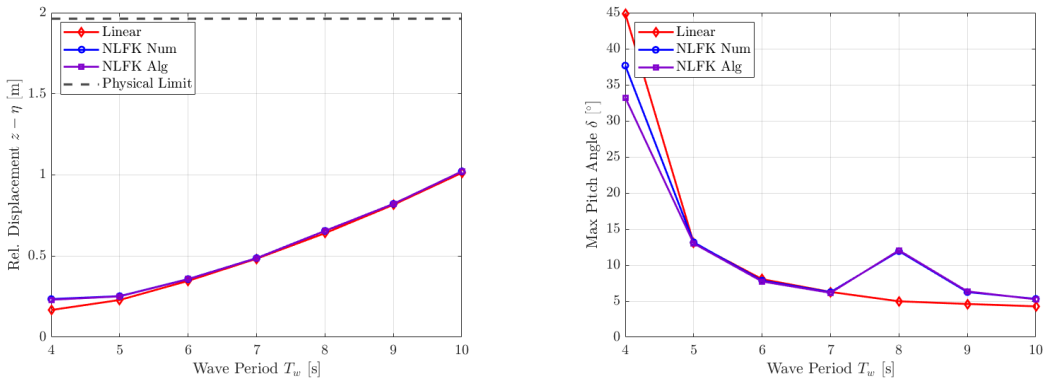


Figure 4.10: Kinematic response for the cylindrical geometry as a function of the wave period (T_w) under constant wave steepness: (left) maximum relative displacement and (right) maximum pitch angle.

Froude-Krylov forces in heave is negligible. However, Figure 4.10 shows a distinctive trend: particularly at the $T_w = 8s$ unlike the linear model, the NLFK models exhibit a local peak. Slight

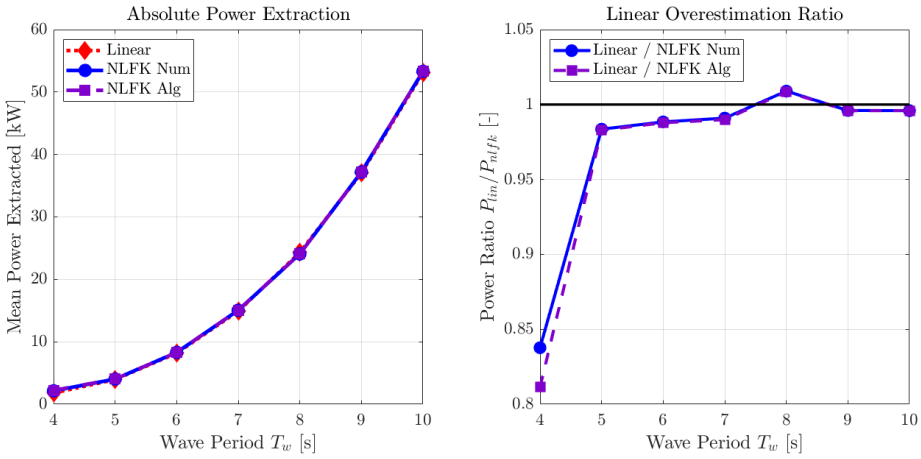


Figure 4.11: Absolute power extraction (left) and power ratio (right) as a function of the wave period T_w for the cylindrical geometry.

differences between the models become evident at the resonance period ($T_w = 4s$), where the linear model overestimates the rotations and underestimates the vertical displacement, leading to an underestimation of the power (Fig. 4.11.)

Sphere

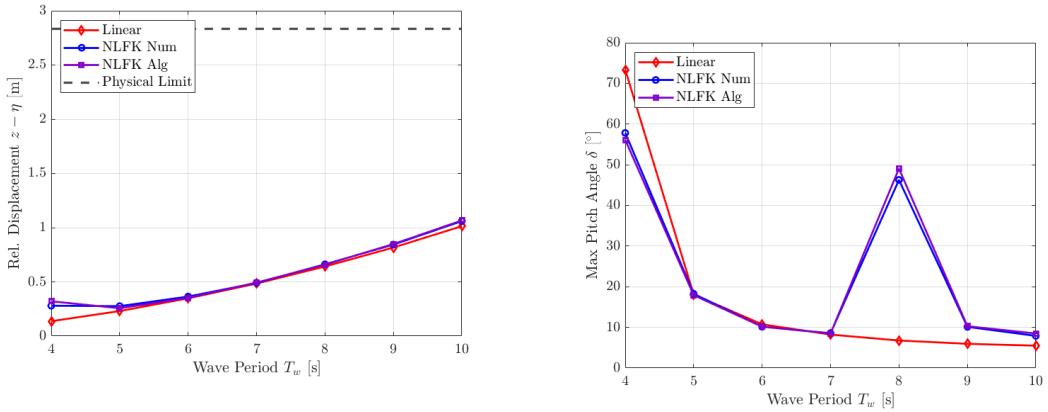


Figure 4.12: Kinematic response for the spherical geometry under passive linear control as a function of the wave period (T_w). Maximum relative displacement (left) and maximum pitch angle (right).

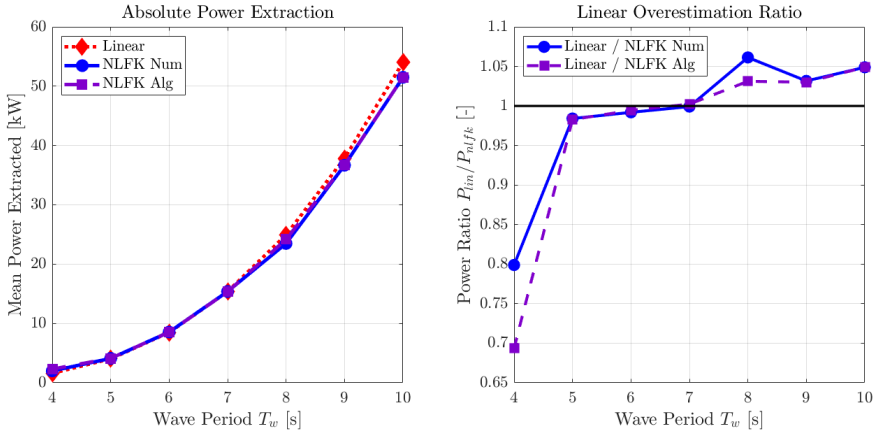


Figure 4.13: Absolute power extraction (left) and power ratio (right) for the Sphere geometry.

As regards the sphere, phenomena similar to those of the cylinder occur at resonance and at the $T_w = 8s$. Given the same displaced volume and water plane area, as shown in the previously sections, the sphere, due to its profile, exhibits a lower stiffness coefficient than that of the cylinder. This means that at the resonance period, the rotations are greater, and even at $T_w = 8s$, the NLFK models are able to capture this instability, which reaches greater angles than in the previous case.
The slight differences observable in the relative displacement and in the comparative power graph are directly linked to the curved profile of the spherical geometry. These non-linear effects are not excessive, as the use of a purely passive control strategy tends to mask these discrepancies. Analysing the results in the figure, at $T = 4s$ the graph showing the ratio of the powers indicates that the linear model underestimates the power by 20–30 per cent compared with the non-linear models. However, looking at the absolute values, the system produces very little energy. Due to resonance, the system causes the buoy to rotate a large amount, but causes it to move very

little vertically. Since the PTO extracts energy only vertically, the power generated is almost zero. Although the NLFK models introduce a large difference in percentage terms, in terms of actual kW this error is negligible.

Spline

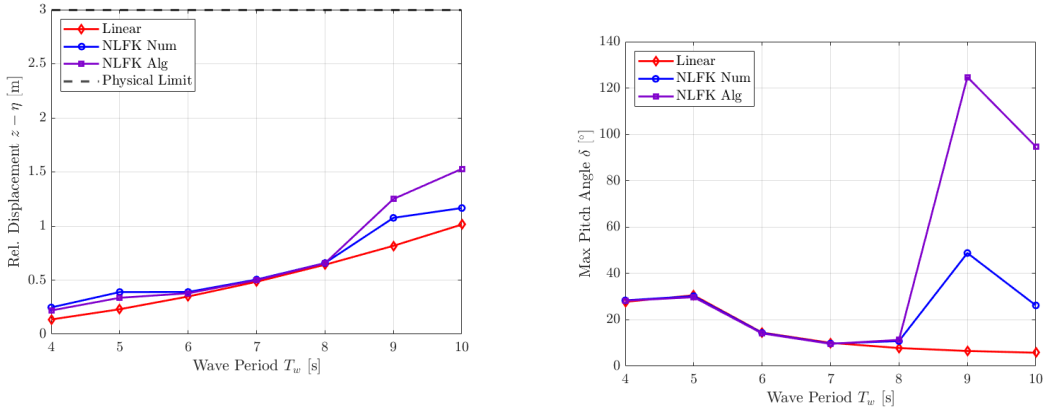


Figure 4.14: Kinematic response for the Spline geometry under passive control.

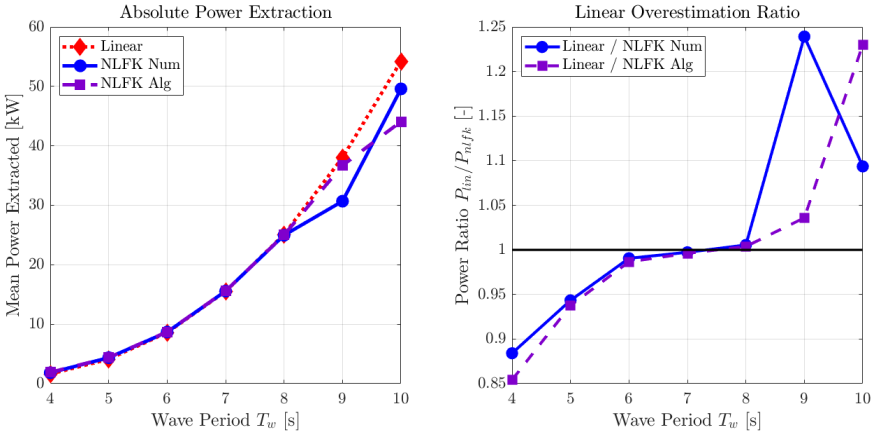


Figure 4.15: Absolute power extraction (left) and corresponding linear overestimation ratio (right) for the Spline geometry under passive linear control.

As can be seen from Figure 4.14, a geometry characterised by a complex profile of revolution exhibits more pronounced variations in relative displacement than predicted by the linear model. Unlike the cases (cylinder and sphere) examined previously, the period at which the rotational instability is triggered is shifted towards $T_w = 9$ s.
The graphs shown so far therefore demonstrate that the FK forces cause instability phenomena in pitch [26].
As the wave period increases, the water wets the volume of the spline asymmetrically, and when subjected to partial emergence, this pitch instability becomes apparent. Although the spline

has a higher radiative damping coefficient than the other geometries, it is characterised by lower hydrostatic stiffness. The results shown imply the need to evaluate the small-angle approximation adopted in the algebraic NLFK model.
It can be seen that for the cylinder this approximation remains largely valid, since the angular excursions remain within limited ranges. As regards the sphere, the approximation holds up even under rotations of 50° thanks to a distinctive and fundamental geometric characteristic: in a perfectly spherical body, the hydrostatic and dynamic pressure vectors always act perpendicular to the wetted surface, pointing constantly towards the centre of the geometry. This means that the line of action of the thrust always intersects the central axis at the same point, keeping the metacentre fixed and coinciding with the geometric centre. The absence of any spatial migration of the metacentre eliminates the serious non-linearities associated with variations in the lever arm. In contrast, the Spline does not possess this symmetry. Large rotations asymmetrically deform the submerged volume, causing a significant shift in the centre of buoyancy and, consequently, a marked migration of the metacentre [27].
Instabilities and non-linear phenomena are also evident from Figure 4.15. At high periods, the linear model—which does not account for pitch instabilities—tends to overestimate the behaviour of the models. To allow the study of larger excursions and to limit pitch rotations that would lead to the collapse of the algebraic model, the stiffness of the mooring system has been increased to $3.5 \times 10^5 Nm/rad$. This measure stiffens the response to extreme rotations during passive control of the spline and, consequently, partially masks the strong non-linear effects in heave, stabilising the dynamics for the subsequent optimisation phases.

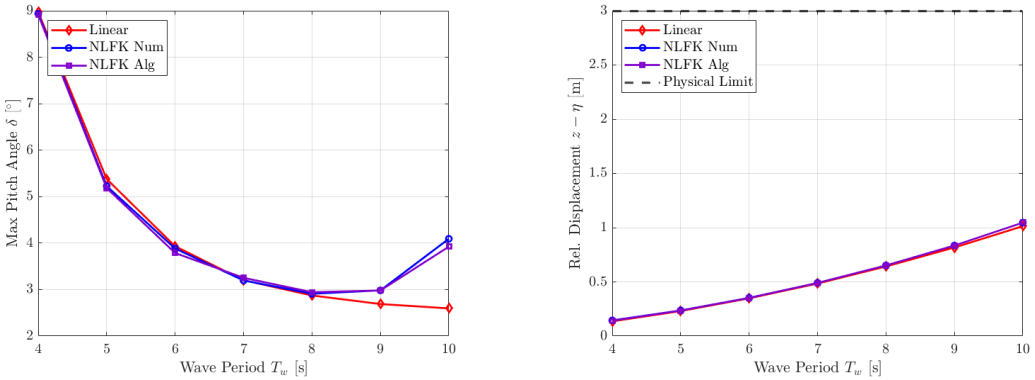


Figure 4.16: Comparison of the maximum pitch angle (left) and the relative displacement (rigth) across varying wave periods for the Linear and NLFK models.

As highlighted in the literature, the non-linear Froude–Krylov forces give rise to anomalous rotational dynamics. The static pitch moment does not remain constant. Consequently, it is shown that when the metacentre drops below the centre of gravity of the device, the static pitch moment changes sign and, rather than acting as a hydrostatic restoring moment towards the equilibrium position, it acts as a capsizing force [16].

4.3.3 Reactive Control

The energy extraction efficiency of a WEC depends heavily on the applied control strategy. Unlike passive control, which relies solely on a linear damping term, reactive control introduces an elastic stiffness component proportional to the displacement. Consequently, the force applied by the PTO system is defined as: [28]

$$F_{PTO} = -K_{pto}z - B_{pto}\dot{z} \tag{4.1}$$

As demonstrated in the literature, the introduction of an elastic component into the system makes it possible to alter the natural frequency of the float, forcing the system into a state of resonance with the incident wave in order to maximise the amplitudes of oscillation. [19]
There are various algorithmic control methods designed to maximise device power; however, for the sake of simplicity – and since it is not the aim of this thesis to design an optimisation algorithm – this section carries out a preliminary parametric investigation to identify a fixed set of stiffness coefficients (K_{pto}) and damping coefficients (B_{pto}). The final values chosen for the simulations are those which, within the explored domain, ensured the maximisation of the average power extracted for the specific geometries analysed.
In order to minimise the computational cost associated , the parametric study of reactive control was focused on a specific sea state ($T_w = 8$ s, $H_w = 1.8$ m) and carried out for all three geometries using linear simulation and the algebraic NLFK model, due to its greater computational speed. Table 4.4 shows the sub-optimal parameter sets that maximise the average power extracted for each geometry under these operating conditions. To ensure the consistency of the simulations, all sets of parameters that would have caused the float to emerge completely were excluded.
Taking into account the effects of pitch instability, as discussed in the previous section, the pitch stiffness coefficient of the mooring ($K_{moor,pitch}$) has been increased to $3.5 \times 10^5 Nm/rad$.

Table 4.4: Reactive control parameters for the different geometries at $T_w = 8$ s, $H_w = 1.8$ m.

	LINEAR		**NLFK**	
Geometry	B_{pto}	K_{pto}	B_{pto}	K_{pto}
Cylinder	8.70×10^4	-1.52×10^5	8.70×10^4	-1.52×10^5
Sphere	6.20×10^4	-1.73×10^5	6.00×10^4	-1.35×10^5
Spline	6.20×10^4	-1.73×10^5	6.20×10^4	-1.31×10^5

Cylinder

As shown in Figure 4.17, the curves relating to vertical displacement show an almost perfect overlap between the linear model and the NLFK models. The cylinder has a constant cross-sectional area throughout its draft. Consequently, the effective area at buoyancy does not undergo any substantial changes during oscillations. The linear model is therefore able to perfectly simulate the behaviour of the cylinder; this is also evident from the parameterisation carried out, as both models suggest the same stiffness and damping values in order to maximise power.
This kinematic consistency is also evident in the graph of extracted power (Fig. 4.19), where no particular differences are apparent between the NLFK and linear models.
However, the analysis of relative displacement (Fig. 4.18) highlights a phase lag induced by the

PTO. The reactive control intervenes by modifying the dynamics of the float; the introduction of the stiffness term causes the float's velocity to come into phase with the excitation force in order to achieve the resonance condition.

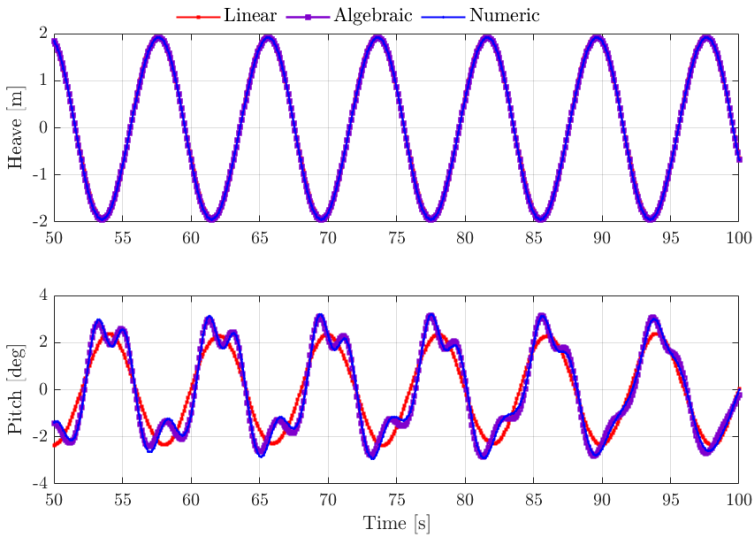


Figure 4.17: Kinematic response in heave (top) and pitch (bottom) for the cylindrical floater under reactive control, comparing Linear, Algebraic, and Numerical models.

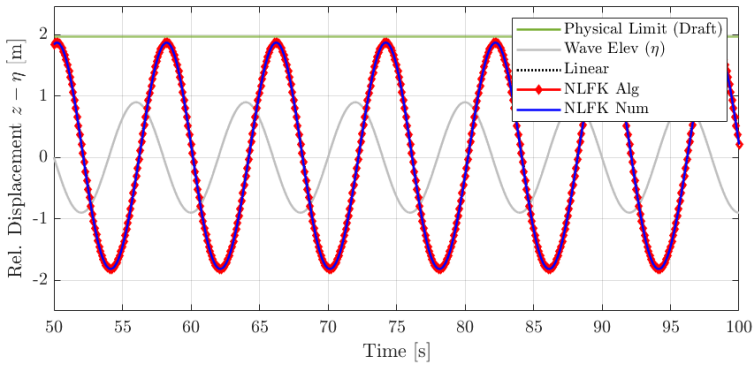


Figure 4.18: Relative heave displacement compared to the wave elevation for the cylindrical geometry.

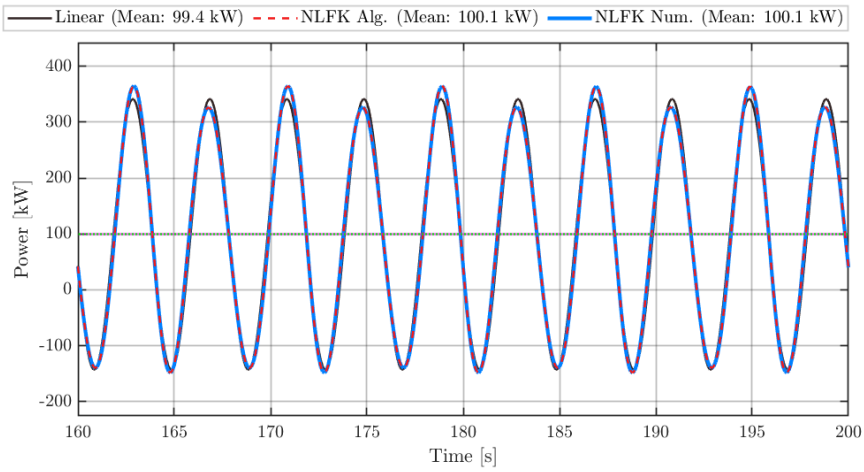


Figure 4.19: Instantaneous power extraction and mean power values under reactive control.

Sphere

In the sphere, the cross-sectional area of the floating section varies during vertical oscillation. The linear model assumes and calculates forces on a constant average surface; as can be seen from Figure 4.20, it overestimates the heave excursions. The NLFK models capture the variation in volume, showing that the actual vertical displacement is smaller. The increase in the stiffness coefficient whilst moored is reflected in the plot of the relative amplitudes of the pitch angle; these are very limited and, as with the cylinder, the algebraic model follows the numerical model perfectly in the sphere as well.

The non-linearity due to the geometric shape is evident in the case of the sphere. The non-linear models, by incorporating the actual distribution of pressures across the geometry, estimate an average power output of 77.4 kW for the algebraic solver and 78.6 kW for the numerical solver. Compared with the linear model, there is a discrepancy of approximately 80 per cent, due to the linear assumption of an unaltered buoyant area, which fails to quantify the alteration of the Froude–Krylov excitation forces during the large vertical oscillations of the spherical float.

Analysing the relative displacement plot (Fig. 4.21), the curve for the linear model describes a symmetrical sinusoidal excursion. On the other hand, the NLFK models reveal a marked asymmetry between the emergence and submergence phases. The peaks of the NLFK relative displacement reach approximately 1.8 m, whilst the troughs extend down to almost -2.5 m. The reason for this behaviour lies in the geometric profile of the buoy under consideration, which increases in diameter towards the equator with depth and then narrows towards the poles. The kinematic asymmetry is evident in the instantaneous power plot (Fig. 4.22). The NLFK power curves do not follow a uniform trend, but exhibit cycles characterised by alternating positive peaks of varying magnitude. This irregularity demonstrates how sudden variations in velocity and position result in instantaneous misalignments with respect to the force applied by the PTO

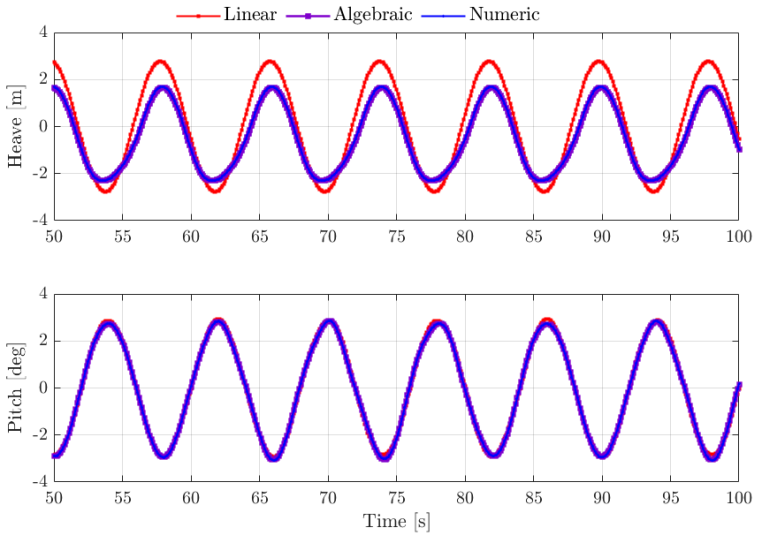


Figure 4.20: Kinematic response in heave (top) and pitch (bottom) for the spherical floater under reactive control, comparing Linear, Algebraic, and Numerical models.

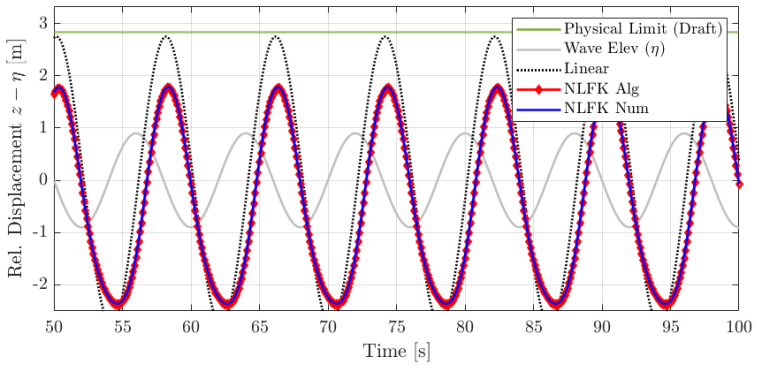


Figure 4.21: Relative heave displacement for the spherical geometry.

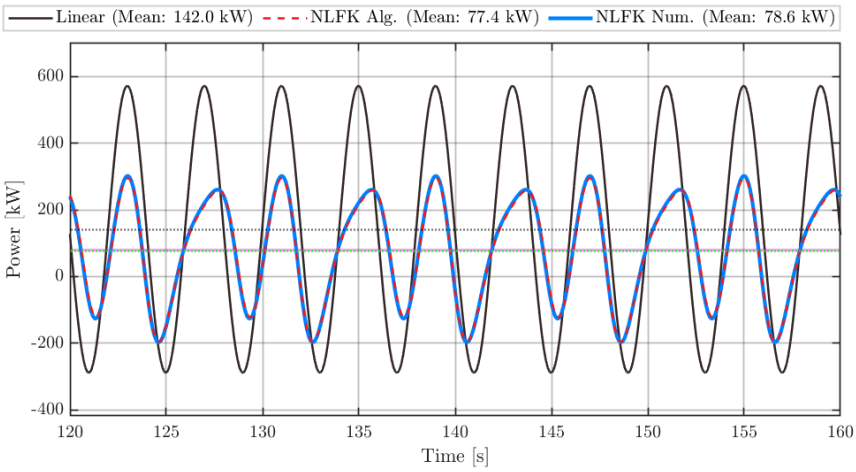


Figure 4.22: Instantaneous power extraction and mean power values under reactive control for the spherical geometry.

Spline

As regards the spline, the most significant effect is evident from the graph of instantaneous and average power (Fig. 4.25). For this geometry, the linear model overestimates the power output, with an average of 147.8 kW. During the optimisation phase, the NLFK model shows a lower PTO stiffness than that obtained from the linear simulation. This difference, but above all the approach to considering the forces acting on a surface of a particular shape, immediately leads to a real average power value of 91.8 kW.
The reason for this overestimation lies in Fig. 4.24. The linear model assumes a movement of up to -2.5 metres. As it cannot see the buoy's profile, the linear model assumes an invariable Archimedes' buoyancy force, leading the controller to believe it can push the buoy to extreme depths to maximise energy.
As the device submerges or surfaces, the cross-sectional area actually varies considerably, leading to a reduction in hydrostatic stiffness. Consequently, the relative displacement shows an asymmetry, in that the positive peaks reach $+1.8m$ whilst the negative ones reach $-2m$.

Simulations carried out under reactive control highlight the delicate balance between hydrodynamic accuracy and computational efficiency. Although the numerical solver based on 2D Simpson's integration guarantees high accuracy, it entails a considerable computational burden. Simulations carried out with 25 regular waves and a time step of $dt = 0.1$ show that runtimes increase dramatically as the complexity of the profile rises, ranging from 8.51 seconds for the cylinder to as much as 229.8 seconds for the Spline geometry (Table 4.5). In contrast, the closed-form algebraic NLFK approach drastically reduces these times, completing the Spline simulation in just 1.46 seconds. This exceptional speed makes the algebraic model an indispensable tool for performing iterative optimisation procedures on the PTO system.

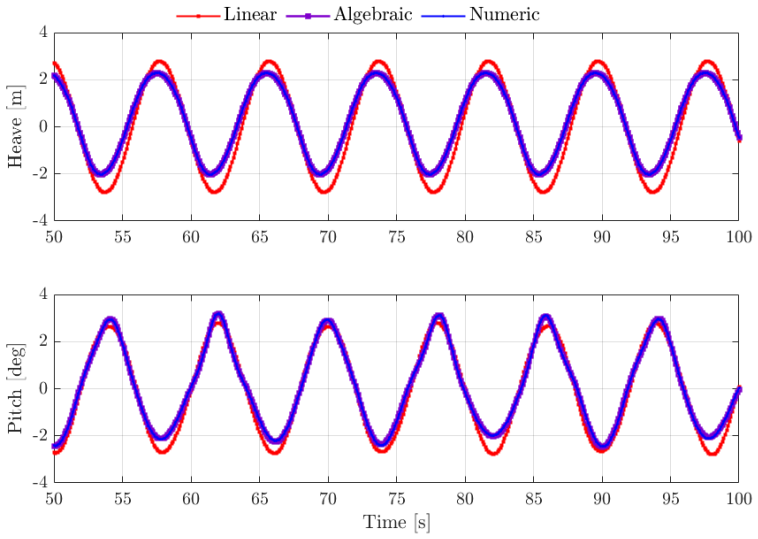


Figure 4.23: Kinematic response in heave (top) and pitch (bottom) for the spline-based floater under reactive control, comparing Linear, Algebraic, and Numerical models.

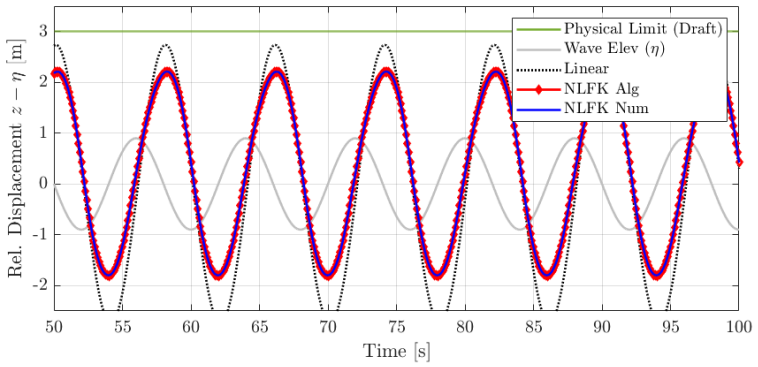


Figure 4.24: Relative heave displacement ($z - \eta$) compared to the wave elevation and the physical draft limit for the spline-based geometry.

Table 4.5: Comparison of computational times between NLFK solvers for the three analyzed geometries.

NLFK Solver	**Cylinder [s]**	**Sphere [s]**	**SplineBuoy [s]**
Algebraic	0.54	0.43	1.46
Numeric	8.51	35.9	229.8

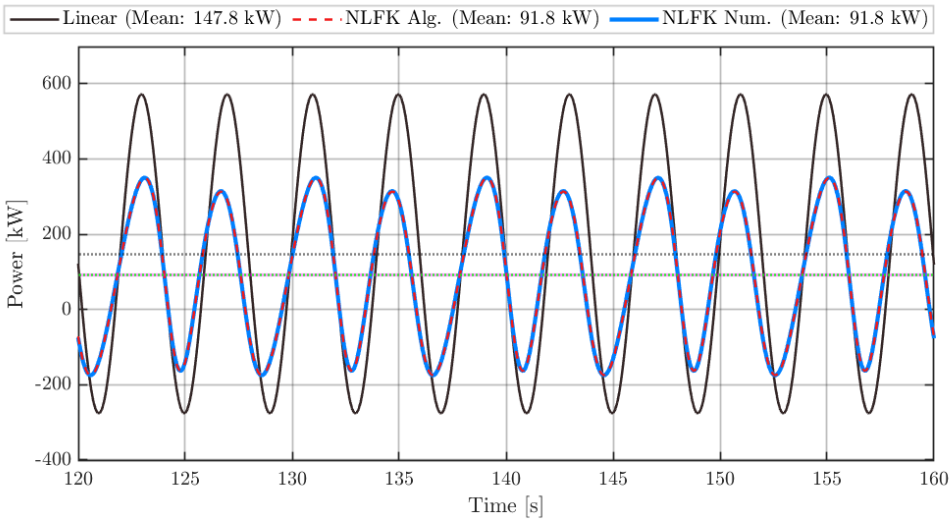


Figure 4.25: Instantaneous power extraction and mean power values under reactive control for the spline-based geometry, highlighting the differences between linear predictions and NLFK models.

Chapter 5

Conclusion

The main objective of this Master's thesis was to overcome the limitations of linear theory as applied to wave energy converters; in particular, the analysis focused on axially symmetric point absorbers.
When a buoy is subjected to large excursions, linear theory tends to overestimate the buoy's displacements, as it is no longer valid to assume a constant wetted surface area along the buoy's profile at large displacements and high wave heights.
To address this problem, this thesis has analysed, by extending the 2021 NLFK4ALL mathematical framework, more complex geometries such as spheres and geometric profiles based on cubic splines, implementing numerical integrations on these geometries using the 2D Simpson's quadrature method, which had previously been applied only to cylindrical and conical sections. Furthermore,in this work the numerical solutions were compared, approaching the geometry and the integration in a completely algebraic manner in order to highlight, specifically for a cylinder, a sphere and a profile based on a cubic spline, the trade-off between accuracy and computational cost.
The toolbox for the new geometries and integration methods has been validated under linear conditions and in irregular waves, taking into account three degrees of freedom (surge, heave and pitch), highlighting how the solutions and approximations for the algebraic method – for example, the assumption of small pitch angles – are necessary in order to solve the integrals using a closed algebraic formula. In order to validate the numerical and algebraic models for the three geometries under consideration, time-domain simulations were carried out. The aim was to analyse the kinematic responses and the power extraction capacity of the device, through the application of a PTO system, as the wave period varied and considering sea states characterised by constant steepness.
The simulations were carried out without control, where the geometries follow the wave motion and the non-linearities due to Froude–Krylov forces do not manifest; moving on to analyses with purely passive control and reactive control. Focusing on the latter, the cylinder—which has a constant cross-sectional area—shows results similar to the linear model, whereas for the spherical and spline-based geometries, the dynamic response varies. When reactive control was applied, the linear model predicted an extracted power of 147.8 kW, whilst the NLFK models revealed an actual average power of 91.8 kW. A similar overestimation error was found for the sphere.
As highlighted in the literature and in this thesis project, the simulations carried out have shown how the non-linear Froude–Krylov forces give rise to significant pitch instabilities. In non-linear simulations, the asymmetric vertical excursion alters the pressure distribution and causes a marked migration of the metacentre.

With regard to the trade-off between accuracy and computational efficiency in this thesis, it has been demonstrated that the numerical model based on Simpson's integration is extremely accurate and stable, but entails very high computational costs as geometric complexity increases. The algebraic approach offers a significant advantage in terms of computational efficiency; however, its validity is closely linked to certain simplifying assumptions. The approximation for small angles of rotation and the truncation of the Maclaurin series can, in fact, trigger instability phenomena, particularly in the high-frequency spectrum.
In conclusion, the work carried out in this thesis offers promising opportunities for future developments. Specifically, the models presented could be extended to:

- Implement even faster and more stable numerical algorithms;
- Develop advanced control strategies and implement faster optimisations;
- Investigate new geometries, by analysing how the dynamic response varies on floats defined by splines with different gradients;

The ultimate aim of this research is to make simulations of wave energy converters (WECs) faster and more accurate, so that these technologies can make a tangible contribution to the development of a more sustainable energy future.

Appendix A

Algebraic Solution

This section contains all the algebraic solutions to the integrals that have been solved for all three geometries.

A.0.1 Main parameters

Defining the fundamental parameters:

- ρ_w, g: water density and gravitational acceleration.
- R_{ij}: elements of the rotation-translation matrix (from *Body-Fixed* to *World-Frame*).
- m, q: parameters of the profile of revolution $f(\rho) = m\rho + q$. For a cylinder $m = 0, f(\rho) = q$.
- ρ_1, ρ_2: integration limits along the local vertical coordinate ρ.
- a_w, ω, k: amplitude, angular frequency, and wave number.
- $\bar{\eta}$: flat approximation of the free surface elevation.
- $k_s = k\frac{\text{depth}}{\bar{\eta}+\text{depth}}$: scaled wave number (*Wheeler stretching*).
- $\chi = kR_{11}$ and $\chi_s = k_s R_{33}$.
- $X_C = R_{14}$: horizontal position in the *World-Frame*.
- Harmonic terms: $T_{\cos} = a_w \cos(\omega t + \phi_w - kX_C)$ and $T_{\sin} = a_w \sin(\omega t + \phi_w - kX_C)$.

A.1 General Approach

To better understand the approach that led to the solution of the Froude–Krylov forces, an example involving a spherical buoy is considered; the various steps leading up to the final result are therefore shown for a buoy subjected to 3 DoF (surge,heave,pitch).
As demonstrated in the previous sections, the wetted surface of the buoy can be parameterised in local cylindrical coordinates (ρ, θ):

$$\hat{x} = f(\rho)\cos\theta, \quad \hat{y} = f(\rho)\sin\theta \tag{A.1}$$

The perfect symmetry of the sphere's profile of revolution leads to the product of the vertical component of the normal vector and the infinitesimal displacement being simplified to the following equation:

$$n_z \, dS = -\rho \, d\theta \, d\rho \tag{A.2}$$

Thanks to the rotation-translation matrix, it is possible to map and convert between the global reference frame (WF) and the local reference frame (BF).
Let $C_1 = R_{14}$ denote the horizontal position of the centre and $C_3 = R_{34}$ the vertical height (elevation) of the centre of the sphere in the global reference frame. The global coordinate z obtained from the rototranslation matrix with respect to the BF reference frames is:

$$z = R_{31}\hat{x} + R_{33}\rho + C_3 \tag{A.3}$$

Substituting the parametrisation of $\hat{x}$, it is obtained:

$$z = R_{31} f(\rho) \cos\theta + R_{33}\rho + C_3 \tag{A.4}$$

The Eq. A.4 is applied to the static and dynamic pressure terms.Therefore, for the static Froude–Kyrlow force in the vertical direction, follows:

$$F_{st,z} = \int_{\varrho_1}^{\varrho_2} \int_{-\pi}^{\pi} \rho_w g \Big(\eta - C_3 - R_{33}\rho - R_{31} f(\rho) \cos\theta \Big) (-\rho) \, d\theta \, d\rho \tag{A.5}$$

When integrating with respect to θ, the term containing $\cos\theta$ cancels out ($\int_{-\pi}^{\pi} \cos\theta \, d\theta = 0$), but the constant terms are multiplied by 2π. The integral becomes:

$$F_{st,z} = 2\pi\rho_w g \int_{\varrho_1}^{\varrho_2} \Big(R_{33}\rho^2 + (C_3 - \eta)\rho \Big) \, d\rho \tag{A.6}$$

The exact algebraic solution for a sphere is:

$$F_{st,z} = 2\pi\rho_w g \left[R_{33}\frac{\rho^3}{3} + (C_3 - \eta)\frac{\rho^2}{2} \right]_{\varrho_1}^{\varrho_2} \tag{A.7}$$

Where ϱ_1 and ϱ_2 are the limits of integration.
As regards the dynamic component of pressure, solving its integral requires certain approximations that are necessary in order to derive a closed-form algebraic expression. The main approximation consists to neglect the term relative to the rotation in pitch, therefore the pressure into BF is:

$$P_{dy,BF} \approx \rho_w g \, a \, e^{k(C_3 + R_{33}\rho - \eta)} \cos(\omega t - kx) \tag{A.8}$$

with $x = R_{11}\hat{x} + C_1$
Associating the cylindrical coordinates to $\hat{x}$ and $\hat{z}$, considering :

- $\Phi_c = \omega t - kC_1$
- $\chi = kR_{11}$
- $c = k_s R_{33}$

The Eq. A.8 becomes:

$$F_{dy,z} = \rho_w g a \int_{\varrho_1}^{\varrho_2} e^{k(C_3 - \eta)} e^{c\rho} (-\rho) \left(\int_{-\pi}^{\pi} \cos\left(\Phi_c - \chi f(\rho) \cos\theta \right) d\theta \right) d\rho \tag{A.9}$$

Considering the integration over the azimuthal angle θ in Eq. A.9, using the trigonometric addition formulas, the argument of the cosine can be expressed as:

$$\int_{-\pi}^{\pi} \Big[\cos(\Phi_c)\cos(\chi f(\rho)\cos\theta) + \sin(\Phi_c)\sin(\chi f(\rho)\cos\theta) \Big] d\theta \tag{A.10}$$

Calculating the integral over the domain $[-\pi, \pi]$ results in the elimination of the second term, which contains the sine function.

$$\cos(\Phi_c) \int_{-\pi}^{\pi} \cos\big(\underbrace{\chi f(\rho)}_{z} \cos\theta \big)\, d\theta \tag{A.11}$$

In order to solve the Eq. A.11, it is necessary to use the Jacobi–Anger expansion. This expansion involves equating the term $\cos(z\cos\theta)$ to an infinite series of Bessel functions. Conceptually, what happens is that a plane wave is transformed into a sum of an infinite number of cylindrical waves. These cylindrical or harmonic waves are Bessel functions of various orders. The general identity of this expansion it is possible found in [29]:

$$e^{iz\cos\theta} = J_0(z) + 2\sum_{n=1}^{\infty} i^n J_n(z)\cos(n\theta) \tag{A.12}$$

[30] shows that the real part of the previous equation can be written as:

$$\cos(z\cos\theta) \equiv J_0(z) + 2\sum_{n=1}^{\infty} (-1)^n J_{2n}(z)\cos(2n\theta) \tag{A.13}$$

The function is subject to various simplifications, since, depending on the degree of freedom considered, the resulting expansion must be multiplied by the corresponding terms of the product **ndS**, as shown in the Eq. 2.55. Integrating these products over a complete domain leads to simplifications due to asymmetries and orthogonality In the implemented 3-degree-of-freedom model, the infinite spectrum of these harmonics is analytically reduced to just two active components. The heave force is governed entirely by the zero-order axisymmetric harmonic, $J_0(z)$, since integration over the azimuthal angle perfectly cancels out the asymmetric contributions, reducing the integral to the following identity:

$$\int_{-\pi}^{\pi} \cos(z\cos\theta)\, d\theta = 2\pi J_0(z) \tag{A.14}$$

On the contrary the surge force and the pitch torque are governed exclusively by the first-order harmonic, $J_1(z)$. All higher-order harmonics ($n \geq 2$) are geometrically orthogonal to the degrees of freedom under consideration and vanish analytically over the entire azimuthal integration domain. As formalised in [31], Bessel functions of the first kind can be represented analytically by an infinite series expansion. In the context of WECs, since $z \ll 1$, it is possible to apply the Maclaurin series to the infinite sum:

$$J_0(z) = \sum_{m=0}^{\infty} \frac{(-1)^m}{(m!)^2} \left(\frac{z}{2}\right)^{2m} \approx 1 - \frac{z^2}{4} + \frac{z^4}{64} - \frac{z^6}{2304} + \dots \tag{A.15}$$

By truncating the series at the first few terms and substituting the spatial argument $z = \chi\sqrt{R_s^2 - \rho^2}$ into the truncated expansion and multiplying it by the projection of the vertical

normal ($-\rho$), the even powers of the polynomial are converted into odd powers. The known terms are then grouped into constant geometric coefficients (c_1, c_3, c_5, c_7):

$$-\rho \cdot 2\pi J_0\left(\chi\sqrt{R_s^2-\rho^2}\right) \approx 2\pi\left(c_1\rho + c_3\rho^3 + c_5\rho^5 + c_7\rho^7\right) \tag{A.16}$$

Finally, by substituting this polynomial expansion back into the original integral over $d\rho$, together with the exponential decay term $e^{c\rho}$, the heave force becomes purely algebraic. By calculating the integrals that can be solved using integration by parts, $E_n(\rho) = \int \rho^n e^{c\rho}\, d\rho$, the simulator is able to evaluate the force instantaneously simply by substituting the geometric contours of the submerged region:

$$F_{dy,z} = 2\pi\rho_w g\, a_w \cos(\Phi_c) e^{k_s(C_3-\eta)} \sum_{n=1,3,5,7} c_n \Big[E_n(\rho)\Big]_{\rho_1}^{\rho_2} \tag{A.17}$$

A.2 Cylinder

Static Forces

The static restoring forces and moments for the cylindrical geometry are given by:

$$F_{st_s} = \rho_w g\pi R_{31} q^2(\rho_2 - \rho_1) \tag{A.18}$$

$$F_{st_sway} = \rho_w g\pi R_{32} q^2(\rho_2 - \rho_1) \tag{A.19}$$

$$F_{st_h} = 0 \tag{A.20}$$

$$T_{st_r_lat} = -\rho_w g\pi R_{32} \frac{q^2}{2}(\rho_2^2 - \rho_1^2) \tag{A.21}$$

$$T_{st_p_lat} = \rho_w g\pi R_{31} \frac{q^2}{2}(\rho_2^2 - \rho_1^2) \tag{A.22}$$

Dynamic Forces

Using the Maclaurin series approximation of the Bessel function, the dynamic coefficient of the cylinder is defined as:

$$C_{cyl} = -\rho_w g\pi q^2 T_{\sin}\left(1 - \frac{\chi^2 q^2}{8} + \frac{\chi^4 q^4}{192} - \frac{\chi^6 q^6}{9216}\right) \tag{A.23}$$

The dynamic forces are then:

$$F_{dy_s} = C_{cyl}\frac{\chi}{\chi_s R_{33}}\left[e^{\chi_s\rho_2 + k_s(R_{34}-\bar{\eta})} - e^{\chi_s\rho_1 + k_s(R_{34}-\bar{\eta})}\right] \tag{A.24}$$

$$F_{dy_h} = 0 \tag{A.25}$$

$$T_{dy_p} = C_{cyl}\frac{\chi}{(\chi_s R_{33})^2}\left[(\chi_s R_{33}\rho_2 - 1)e^{\chi_s\rho_2 + k_s(R_{34}-\bar{\eta})} - (\chi_s R_{33}\rho_1 - 1)e^{\chi_s\rho_1 + k_s(R_{34}-\bar{\eta})}\right] \tag{A.26}$$

A.3 Cone

Static Forces

The primitives required for the static geometric integration are:

$$P_{R2}(\rho) = \frac{m^2}{3}\rho^3 + mq\rho^2 + q^2\rho \tag{A.27}$$

$$P_{PR}(\rho) = \frac{m^4+m^2}{4}\rho^4 + \frac{mq(3m^2+2)}{3}\rho^3 + \frac{q^2(3m^2+1)}{2}\rho^2 + mq^3\rho \tag{A.28}$$

$$I_{sth}(\rho) = R_{33}m\frac{\rho^3}{3} + (R_{33}q + R_{34}m)\frac{\rho^2}{2} + R_{34}q\rho \tag{A.29}$$

Evaluating these between the limits ρ_1 and ρ_2 yields the static loads:

$$F_{st_s} = \rho_w g\pi R_{31}\big[P_{R2}(\rho_2) - P_{R2}(\rho_1)\big] \tag{A.30}$$

$$F_{st_sway} = \rho_w g\pi R_{32}\big[P_{R2}(\rho_2) - P_{R2}(\rho_1)\big] \tag{A.31}$$

$$F_{st_h} = -2\rho_w g\pi m\big[I_{sth}(\rho_2) - I_{sth}(\rho_1)\big] \tag{A.32}$$

$$T_{st_p_lat} = \rho_w g\pi R_{31}\big[P_{PR}(\rho_2) - P_{PR}(\rho_1)\big] \tag{A.33}$$

$$T_{st_r_lat} = -\rho_w g\pi R_{32}\big[P_{PR}(\rho_2) - P_{PR}(\rho_1)\big] \tag{A.34}$$

Dynamic Forces

The dynamic force expansion generates polynomial-exponential integrals $I_n(\rho)$. For $n \in [1, 9]$, the general expression is:

$$I_n(\rho) = \frac{e^{\chi_s\rho + k_s(R_{34}-\bar{\eta})}}{\chi_s}\sum_{j=0}^{n}(-1)^j\frac{n!}{(n-j)!}\left(\frac{m}{\chi_s}\right)^j(m\rho+q)^{n-j} \tag{A.35}$$

For instance, the first three integrals are:

$$I_1(\rho) = \frac{e^{\cdots}}{\chi_s}\left[(m\rho+q) - \frac{m}{\chi_s}\right] \tag{A.36}$$

$$I_2(\rho) = \frac{e^{\cdots}}{\chi_s}\left[(m\rho+q)^2 - \frac{2m}{\chi_s}(m\rho+q) + \frac{2m^2}{\chi_s^2}\right] \tag{A.37}$$

$$I_3(\rho) = \frac{e^{\cdots}}{\chi_s}\left[(m\rho+q)^3 - \frac{3m}{\chi_s}(m\rho+q)^2 + \frac{6m^2}{\chi_s^2}(m\rho+q) - \frac{6m^3}{\chi_s^3}\right] \tag{A.38}$$

Letting $\Delta I_n = I_n(\rho_2) - I_n(\rho_1)$, the dynamic forces become:

$$F_{dy_h} = \rho_w g\pi m T_{\cos}\left(2\Delta I_1 - \frac{\chi^2}{2}\Delta I_3 + \frac{\chi^4}{32}\Delta I_5 - \frac{\chi^6}{1152}\Delta I_7\right) \tag{A.39}$$

$$F_{dy_s} = -\rho_w g\pi\chi T_{\sin}\left(\Delta I_2 - \frac{\chi^2}{8}\Delta I_4 + \frac{\chi^4}{192}\Delta I_6 - \frac{\chi^6}{9216}\Delta I_8\right) \tag{A.40}$$

Introducing the combined term $\Delta J_n = \frac{m^2+1}{m}\Delta I_{n+1} - \frac{q}{m}\Delta I_n$, the dynamic pitch moment is:

$$T_{dy_p} = -\rho_w g\pi\chi T_{\sin}\left(\Delta J_2 - \frac{\chi^2}{8}\Delta J_4 + \frac{\chi^4}{192}\Delta J_6 - \frac{\chi^6}{9216}\Delta J_8\right) \tag{A.41}$$

A.4 Disk

The horizontal bases are treated using polar coordinates. Let z_0 and R_d be the local elevation and radius of the disk in the *Body-Fixed Frame*. The normal direction is defined by $\text{sign}_{n3} \in \{-1, 1\}$ (e.g., 1 for the bottom base, -1 for the top). The *World-Frame* coordinates of the disk center are $z_{WF} = R_{33}z_0 + R_{34}$ and $X_C = R_{13}z_0 + R_{14}$.

Static Forces

The static loads are given by:

$$F_{st_h_disc} = -\rho_w g\pi R_d^2 z_{WF} \cdot \text{sign}_{n3} \tag{A.42}$$

$$T_{st_r_disc} = -\text{sign}_{n3}\rho_w g\pi \frac{R_d^4}{4} R_{32} \tag{A.43}$$

$$T_{st_p_disc} = \text{sign}_{n3}\rho_w g\pi \frac{R_d^4}{4} R_{31} \tag{A.44}$$

Dynamic Forces

Integrating the dynamic pressure with the expanded Bessel function yields:

$$F_{dy_disc} = \text{sign}_{n3}\rho_w g\pi R_d^2 e^{k_s(z_{WF}-\bar{\eta})} T_{\cos}\left(1 - \frac{\chi^2 R_d^2}{8} + \frac{\chi^4 R_d^4}{192} - \frac{\chi^6 R_d^6}{9216}\right) \tag{A.45}$$

$$T_{dy_p_disc} = -\text{sign}_{n3}\frac{1}{4}\rho_w g\pi R_d^4 \chi e^{k_s(z_{WF}-\bar{\eta})} T_{\sin}\left(1 - \frac{\chi^2 R_d^2}{12} + \frac{\chi^4 R_d^4}{384}\right) \tag{A.46}$$

A.5 Sphere

Consider a spherical portion of radius R_s, whose center is offset by z_{0_sph} along the vertical axis of the *Body-Fixed Frame*. The center coordinates in the *World-Frame* are $Z_C = R_{33}z_{0_sph} + R_{34}$ and $X_C = R_{13}z_{0_sph} + R_{14}$.
To compute the integrals, the variable change $u = z - z_{0_sph}$ is applied, with integration limits $u_{\min}$ and $u_{\max}$ defined by the free-surface intersections.

Static Forces

The static primitives are:

$$I_{sth_sph}(u) = R_{33}\frac{u^3}{3} + Z_c\frac{u^2}{2} \tag{A.47}$$

$$I_{sts_sph}(u) = R_s^2 u - \frac{u^3}{3} \tag{A.48}$$

Denoting the variation between $u_{\min}$ and $u_{\max}$ as ΔI, the static loads are:

$$F_{st_h_sph} = 2\pi\rho_w g\Delta I_{sth_sph} \tag{A.49}$$

$$F_{st_s_sph} = \pi\rho_w g R_{31}\Delta I_{sts_sph} \tag{A.50}$$

$$F_{st_sway_sph} = \pi\rho_w g R_{32}\Delta I_{sts_sph} \tag{A.51}$$

$$T_{st_p_sph} = z_{0_sph}F_{st_s_sph} \tag{A.52}$$

$$T_{st_r_sph} = -z_{0_sph}F_{st_sway_sph} \tag{A.53}$$

Dynamic Forces

Setting $c = \chi_s$, the dynamic integration produces the exponential-polynomial functions:

$$E_n(u) = \frac{e^{cu} e^{k_s(Z_c - \bar{\eta})}}{c^{n+1}} P_n(cu) \tag{A.54}$$

where $P_n(x)$ are polynomials (e.g., $P_0(x) = 1$, $P_1(x) = x - 1$, $P_2(x) = x^2 - 2x + 2$, up to $n = 8$).

The heave force coefficients c_n are:

$$\begin{aligned}
c_1 &= -1 + \frac{\chi^2}{4} R_s^2 - \frac{\chi^4}{64} R_s^4 + \frac{\chi^6}{2304} R_s^6 \\
c_3 &= -\frac{\chi^2}{4} + 2\frac{\chi^4}{64} R_s^2 - 3\frac{\chi^6}{2304} R_s^4 \\
c_5 &= -\frac{\chi^4}{64} + 3\frac{\chi^6}{2304} R_s^2 \\
c_7 &= -\frac{\chi^6}{2304}
\end{aligned}$$

yielding the heave force:

$$F_{dy_h_sph} = 2\pi\rho_w g T_{\cos}\big(c_1 \Delta E_1 + c_3 \Delta E_3 + c_5 \Delta E_5 + c_7 \Delta E_7\big) \tag{A.55}$$

Similarly, the horizontal force coefficients s_n are:

$$\begin{aligned}
s_0 &= \chi R_s^2 - \frac{\chi^3}{8} R_s^4 + \frac{\chi^5}{192} R_s^6 - \frac{\chi^7}{9216} R_s^8 \\
s_2 &= -\chi + 2\frac{\chi^3}{8} R_s^2 - 3\frac{\chi^5}{192} R_s^4 + 4\frac{\chi^7}{9216} R_s^6 \\
s_4 &= -\frac{\chi^3}{8} + 3\frac{\chi^5}{192} R_s^2 - 6\frac{\chi^7}{9216} R_s^4 \\
s_6 &= -\frac{\chi^5}{192} + 4\frac{\chi^7}{9216} R_s^2 \\
s_8 &= -\frac{\chi^7}{9216}
\end{aligned}$$

giving the surge force and pitch moment:

$$F_{dy_s_sph} = -\pi\rho_w g T_{\sin}\big(s_0 \Delta E_0 + s_2 \Delta E_2 + s_4 \Delta E_4 + s_6 \Delta E_6 + s_8 \Delta E_8\big) \tag{A.56}$$

$$T_{dy_p_sph} = z_{0_sph} F_{dy_s_sph} \tag{A.57}$$

A.6 Cubic Spline

The revolution profile is a cubic polynomial of the local vertical coordinate ρ:

$$f(\rho) = a\rho^3 + b\rho^2 + c\rho + d \tag{A.58}$$

Based on the exact geometric vectors, the horizontal and vertical normal components scale with $f(\rho)$ and $f(\rho)f'(\rho)$, respectively. The cross product for the rotational moments introduces $f(\rho)f'(\rho)+\rho$. The dynamic pressure variation is represented by truncating the Taylor expansions of the Bessel functions to the first two terms to ensure numerical stability. The vertical field

(J_0) introduces terms proportional to 1 and $f(\rho)^2$, while the horizontal field (J_1) introduces $f(\rho)$ and $f(\rho)^3$.
Multiplying the geometric kernels by the truncated pressure terms yields a set of computationally efficient polynomials:

$$A(\rho) = f(\rho)f'(\rho) \quad \text{(Degree 5)} \tag{A.59}$$
$$B(\rho) = f(\rho)^2 \quad \text{(Degree 6)} \tag{A.60}$$
$$C(\rho) = f(\rho)^3 f'(\rho) \quad \text{(Degree 11)} \tag{A.61}$$
$$D(\rho) = f(\rho)^4 \quad \text{(Degree 12)} \tag{A.62}$$
$$P(\rho) = C(\rho) + \rho B(\rho) \quad \text{(Degree 11)} \tag{A.63}$$
$$Q(\rho) = f(\rho)^5 f'(\rho) + \rho D(\rho) \quad \text{(Degree 17)} \tag{A.64}$$

Static Forces

The static loads are determined by analytically integrating the hydrostatic pressure over $[\rho_1, \rho_2]$. Defining $P_B(\rho)$ as the exact primitive of $B(\rho) = f(\rho)^2$:

$$P_B(\rho) = \int B(\rho)d\rho = \frac{a^2}{7}\rho^7 + \frac{2ab}{6}\rho^6 + \cdots + d^2\rho \tag{A.65}$$

Applying integration by parts, the exact primitives for the static heave (P_H) and pitch/roll (P_{P_stat}) become:

$$P_H(\rho) = \frac{1}{2}(R_{33}\rho + R_{34})f(\rho)^2 - \frac{1}{2}R_{33}P_B(\rho) \tag{A.66}$$

$$P_{P_stat}(\rho) = \frac{1}{4}f(\rho)^4 + \int \rho B(\rho)d\rho \tag{A.67}$$

Evaluating between ρ_1 and ρ_2, the static Froude-Krylov loads are:

$$F_{st_s} = \rho_w g\pi R_{31}[P_B(\rho_2) - P_B(\rho_1)] \tag{A.68}$$
$$F_{st_sway} = \rho_w g\pi R_{32}[P_B(\rho_2) - P_B(\rho_1)] \tag{A.69}$$
$$F_{st_h} = -2\rho_w g\pi[P_H(\rho_2) - P_H(\rho_1)] \tag{A.70}$$
$$T_{st_p_lat} = \rho_w g\pi R_{31}[P_{P_stat}(\rho_2) - P_{P_stat}(\rho_1)] \tag{A.71}$$
$$T_{st_r_lat} = -\rho_w g\pi R_{32}[P_{P_stat}(\rho_2) - P_{P_stat}(\rho_1)] \tag{A.72}$$

Dynamic Forces

Evaluating the Bessel functions at $z = \chi f(\rho)$, the expansions are truncated to the first two terms ($\mathcal{O}(\chi^2)$ for Heave, $\mathcal{O}(\chi^3)$ for Surge/Pitch).

For the vertical dynamics, governed by J_0:

$$J_0(\chi f(\rho)) = \sum_{m=0}^{\infty} \frac{(-1)^m}{(m!)^2}\left(\frac{\chi f(\rho)}{2}\right)^{2m} \approx 1 - \frac{\chi^2}{4}f(\rho)^2 \tag{A.73}$$

For the horizontal and rotational dynamics, governed by J_1:

$$J_1(\chi f(\rho)) = \sum_{m=0}^{\infty} \frac{(-1)^m}{m!(m+1)!}\left(\frac{\chi f(\rho)}{2}\right)^{2m+1} \approx \frac{\chi}{2}f(\rho) - \frac{\chi^3}{16}f(\rho)^3 \tag{A.74}$$

Factoring out $\frac{\chi}{2}$, the polynomial core integrating with the normal vectors is explicitly:

$$J_1(\chi f(\rho)) \propto f(\rho) - \frac{\chi^2}{8} f(\rho)^3 \tag{A.75}$$

Defining $dE_n = \int_{\rho_1}^{\rho_2} \rho^n e^{\chi_s \rho} d\rho$, the integrals are solved algebraically. Letting $I_A, I_B, I_C, I_D, I_P, I_Q$ denote the scalar integration of the corresponding polynomials with dE_n, the closed-form dynamic loads are:

$$F_{dy_h} = 2\pi\rho_w g T_{cos} \left(I_A - \frac{\chi^2}{4} I_C \right) \tag{A.76}$$

$$F_{dy_s} = -\pi\rho_w g \chi T_{sin} \left(I_B - \frac{\chi^2}{8} I_D \right) \tag{A.77}$$

$$T_{dy_p} = -\pi\rho_w g \chi T_{sin} \left(I_P - \frac{\chi^2}{8} I_Q \right) \tag{A.78}$$

Bibliography

[1] A. F. d. O. Falcão, "Wave energy utilization: A review of the technologies," *Renewable and Sustainable Energy Reviews*, vol. 14, no. 3, pp. 899–918, 2010.

[2] S. Al-Sahlawi, G. Seamus, and K. Johnson, "Steady-state harmonic and time domain point absorber modelling," *American Journal of Geospatial Technology (AJGT)*, vol. 3, no. 1, pp. 35–45, 2024.

[3] I. López, J. Andreu, S. Ceballos, I. Martínez de Alegría, and I. Kortabarria, "Review of wave energy technologies and the necessary power-equipment," *Renewable and Sustainable Energy Reviews*, vol. 27, pp. 413–434, 2013.

[4] J. Widén, N. Carpman, V. Castellucci, D. Lingfors, J. Olauson, F. Remouit, M. Bergkvist, M. Grabbe, and R. Waters, "Variability assessment and forecasting of renewables: A review for solar, wind, wave and tidal resources," *Renewable and Sustainable Energy Reviews*, vol. 44, pp. 356–375, 2015.

[5] J. J. Wu, V. Vijayamohan, and R. W. Field, "On the potential of ocean energy technologies to contribute to future sustainability," *Discover Sustainability*, vol. 6, no. 1, p. 741, 2025.

[6] IRENA and OEE, "Scaling up investments in ocean energy technologies," tech. rep., International Renewable Energy Agency (IRENA) and Ocean Energy Europe (OEE), Abu Dhabi, 2023.

[7] B. Guo, T. Wang, S. Jin, S. Duan, K. Yang, and Y. Zhao, "A review of point absorber wave energy converters," *Journal of Marine Science and Engineering*, vol. 10, no. 10, p. 1534, 2022.

[8] G. Giorgi and J. V. Ringwood, "Relevance of pressure field accuracy for nonlinear froude–krylov force calculations for wave energy devices," 2017.

[9] A. Babarit, G. Delhommeau, and P. Ferrant, "On the numerical modelling of the non linear behaviour of a wave energy converter," in *Volume 4: Ocean Space Utilization; Ocean Renewable Energy*, pp. 553–561, ASME, 2009.

[10] G. Giorgi, G. Bracco, and G. Mattiazzo, "Nlfk4all: An open-source demostration toolbox for computationally efficient nonlinear froude-krylov force calculations," in *Atti di convegno*, 2021.

[11] L. Papillon, R. Costello, and J. V. Ringwood, "Boundary element and integral methods in potential flow theory: a review with a focus on wave energy applications," *Journal of Ocean Engineering and Marine Energy*, vol. 6, pp. 303–337, 2020.

[12] D. Cong, J. Shang, Z. Luo, C. Sun, and W. Wu, "Energy efficiency analysis of multi-type floating bodies for a novel heaving point absorber with application to low-power unmanned ocean device," *Energies*, vol. 11, no. 12, p. 3282, 2018.

[13] F. Ardhuin, "Ocean waves in geosciences - parts 1 and 2: general wave topics from deep to shallow water." Laboratoire d'Océanographie Physique et Spatiale, Brest, France, August 2024. August 19, 2024.

[14] W. Cummins, "The impulse response function and ship motion," *Schiffstechnik*, vol. 9, pp. 101–109, 1962.

[15] B. Bosma, Z. Zhang, T. K. A. Brekken, H. T. Özkan-Haller, C. McNatt, and S. C. Yim, "Wave energy converter modeling in the frequency domain: A design guide," IEEE, 2012.

[16] G. Giorgi and J. V. Ringwood, "Analytical representation of nonlinear froude-krylov forces for 3-dof point absorbing wave energy devices," *Ocean Engineering*, vol. 164, pp. 749–759, 2018.

[17] L. F. Shampine, "Matlab program for quadrature in 2d," *Applied Mathematics and Computation*, vol. 202, no. 1, pp. 266–274, 2008.

[18] O. Kayode, O. A. Koya, and T. O. Ajewole, "Determination of the optimal buoy shape for a concept wave energy converter to harness low amplitude sea waves using numerical simulation," *International Journal of Marine Engineering Innovation and Research*, vol. 4, pp. 164–173, September 2019.

[19] J. Falnes, *Ocean Waves and Oscillating Systems: Linear Interactions Including Wave-Energy Extraction*. Cambridge University Press, 2002.

[20] E. Cheever, "Second order runge-kutta." Linear Physical Systems Analysis, Swarthmore College, 2022. Accesso effettuato il: September 14, 2026.

[21] T. I. Fossen, *Handbook of marine craft hydrodynamics and motion control*. Chichester, West Sussex, PO19 8SQ, United Kingdom: John Wiley & Sons, 2011.

[22] H. Abdulkadir and O. Abdelkhalik, "Control co-design optimization of nonlinear wave energy converters," *Ocean Engineering*, vol. 304, p. 117827, 2024.

[23] A. Hasanvand, "Bézier curve." Department of Applied Mathematics, University of Tehran, July 2021. July 2, 2021.

[24] M. Peñalba Retes, A. Mérigaud, J.-C. Gilloteaux, and J. V. Ringwood, "Nonlinear froude-krylov force modelling for two heaving wave energy point absorbers," in *Proceedings of the 11th European Wave and Tidal Energy Conference (EWTEC)*, (Nantes, France), September 2015.

[25] R. Ekström, B. Ekergård, and M. Leijon, "Electrical damping of linear generators for wave energy converters—a review," *Renewable and Sustainable Energy Reviews*, vol. 42, pp. 116–128, 2015.

[26] K. R. Tarrant, *Numerical Modelling of Parametric Resonance of a Heaving Point Absorber Wave Energy Converter*. PhD thesis, Department of Mechanical & Manufacturing Engineering, Trinity College Dublin, March 2015.

[27] A. Biran and R. I. Pulido, *Ship Hydrostatics and Stability*. Butterworth-Heinemann, 2013.

[28] E. Anderlini, D. I. M. Forehand, E. Bannon, Q. Xiao, and M. Abusara, "Reactive control of a two-body point absorber using reinforcement learning," *Ocean Engineering*, vol. 148, pp. 650–658, 2018.

[29] E. W. Weisstein, "Jacobi-Anger Expansion. From MathWorld—A Wolfram Web Resource." [Online; accessed September 14, 2026].

[30] M. Abramowitz and I. A. Stegun, *Handbook of Mathematical Functions with Formulas, Graphs, and Mathematical Tables*. National Bureau of Standards Applied Mathematics Series 55, Washington, D.C.: United States Department of Commerce, 1964.

[31] E. W. Weisstein, "Bessel Function of the First Kind. From MathWorld—A Wolfram Web Resource." [Online; accessed September 14, 2026].